1-12-2021

# Dynamic shifts in the composition of resident and recruited macrophages influence tissue remodeling in NASH

Sabine Daemen

Anastasiia Gainullina

Gowri Kalugotla

Li He

Mandy M Chan

*See next page for additional authors*

## Authors

Sabine Daemen, Anastasiia Gainullina, Gowri Kalugotla, Li He, Mandy M Chan, Joseph W Beals, Kim H Liss, Samuel Klein, Ariel E Feldstein, Brian N Finck, Maxim N Artyomov, and Joel D Schilling

Cell Reports

CellPress
OPEN ACCESS

Article

# Dynamic Shifts in the Composition of Resident and Recruited Macrophages Influence Tissue Remodeling in NASH

Sabine Daemen,[1,2] Anastasiia Gainullina,[2,5] Gowri Kalugotla,[1,2] Li He,[1] Mandy M. Chan,[2] Joseph W. Beals,[4] Kim H. Liss,[1,2,4] Samuel Klein,[4] Ariel E. Feldstein,[6] Brian N. Finck,[1,2,4] Maxim N. Artyomov,[2] and Joel D. Schilling[1,2,3,4,7,*]

[1]Diabetes Research Center, Washington University School of Medicine, St. Louis, MO, USA
[2]Department of Medicine, Washington University School of Medicine, St. Louis, MO, USA
[3]Department of Pathology and Immunology, Washington University School of Medicine, St. Louis, MO, USA
[4]Center for Human Nutrition, Washington University School of Medicine, St. Louis, MO, USA
[5]ITMO University, Saint Petersburg, Russia
[6]Department of Pediatrics, University of California, San Diego, San Diego, CA, USA
[7]Lead Contact
*Correspondence: schillij@wustl.edu
https://doi.org/10.1016/j.celrep.2020.108626

## SUMMARY

Macrophage-mediated inflammation is critical in the pathogenesis of non-alcoholic steatohepatitis (NASH). Here, we describe that, with high-fat, high-sucrose-diet feeding, mature TIM4$^{pos}$ Kupffer cells (KCs) decrease in number, while monocyte-derived Tim4$^{neg}$ macrophages accumulate. In concert, monocyte-derived infiltrating macrophages enter the liver and consist of a transitional subset that expresses *Cx3cr1*/*Ccr2* and a second subset characterized by expression of *Trem2*, *Cd63*, *Cd9*, and *Gpmnb*; markers ascribed to lipid-associated macrophages (LAMs). The *Cx3cr1*/*Ccr2*-expressing macrophages, referred to as C-LAMs, localize to macrophage aggregates and hepatic crown-like structures (hCLSs) in the steatotic liver. In C-motif chemokine receptor 2 (*Ccr2*)-deficient mice, C-LAMs fail to appear in the liver, and this prevents hCLS formation, reduces LAM numbers, and increases liver fibrosis. Taken together, our data reveal dynamic changes in liver macrophage subsets during the pathogenesis of NASH and link these shifts to pathologic tissue remodeling.

## INTRODUCTION

Non-alcoholic fatty liver disease (NAFLD) represents a spectrum of liver abnormalities, including an increase in intrahepatic lipid content (i.e., steatosis) with or without inflammation and fibrosis (i.e., nonalcoholic steatohepatitis [NASH]). NASH is common in people with obesity and diabetes and accounts for an increasing number of patients with cirrhosis and liver failure (Fabbrini et al., 2010; Vernon et al., 2011; Wree et al., 2013). Macrophages are thought to play an important role in the initiation and propagation of liver inflammation and the regulation of liver fibrosis (Kazankov et al., 2019). However, the cellular and molecular pathways that regulate these events are poorly understood and controversial. This is particularly relevant given the heterogeneity of monocyte and macrophage populations that exist in homeostasis and disease.

Kupffer cells (KCs) are the resident macrophages in the liver. These macrophages are predominantly yolk-sac derived and are capable of self-renewal (Schulz et al., 2012). They reside in the liver sinusoids where they play a critical role in phagocytosis of blood-borne toxins/particulates (Gomez Perdiguero et al., 2015; Rogoff and Lipsky, 1981). Liver monocytes and monocyte-derived macrophages (MdMs) are short-lived cells and are present at low levels during physiologic conditions. Resident KCs can be distinguished from MdMs based on a number of cell markers. KCs are F4/80$^{hi}$ and CD11b$^{int}$, whereas monocytes and MdMs tend to be CD11b$^{hi}$ and F4/80$^{int}$ (Guillot and Tacke, 2019). KCs do not express CCR2 or CX3CR1, whereas these surface receptors tend to be abundantly expressed on MdMs (Yona et al., 2013). More recently, specific markers of KCs have been identified including TIM4, CLEC4F, and VSIG4 (Beattie et al., 2016; Scott et al., 2016). Monocytes do not contribute to the KC pool under homeostatic conditions; however, if KCs are depleted, monocyte-derived cells can enter the KC niche and take on the majority of KC features, including CLEC4F and VSIG4 expression (Beattie et al., 2016; Scott et al., 2016). TIM4 expression is delayed in these monocyte-derived cells, allowing for the identification of CLEC4F$^{pos}$, TIM4$^{neg}$ monocyte-derived KCs (Mo-KCs) (Bonnardel et al., 2019; Sakai et al., 2019; Scott et al., 2016).

The biologic heterogeneity and interplay between recruited and resident macrophages in NASH have been difficult to

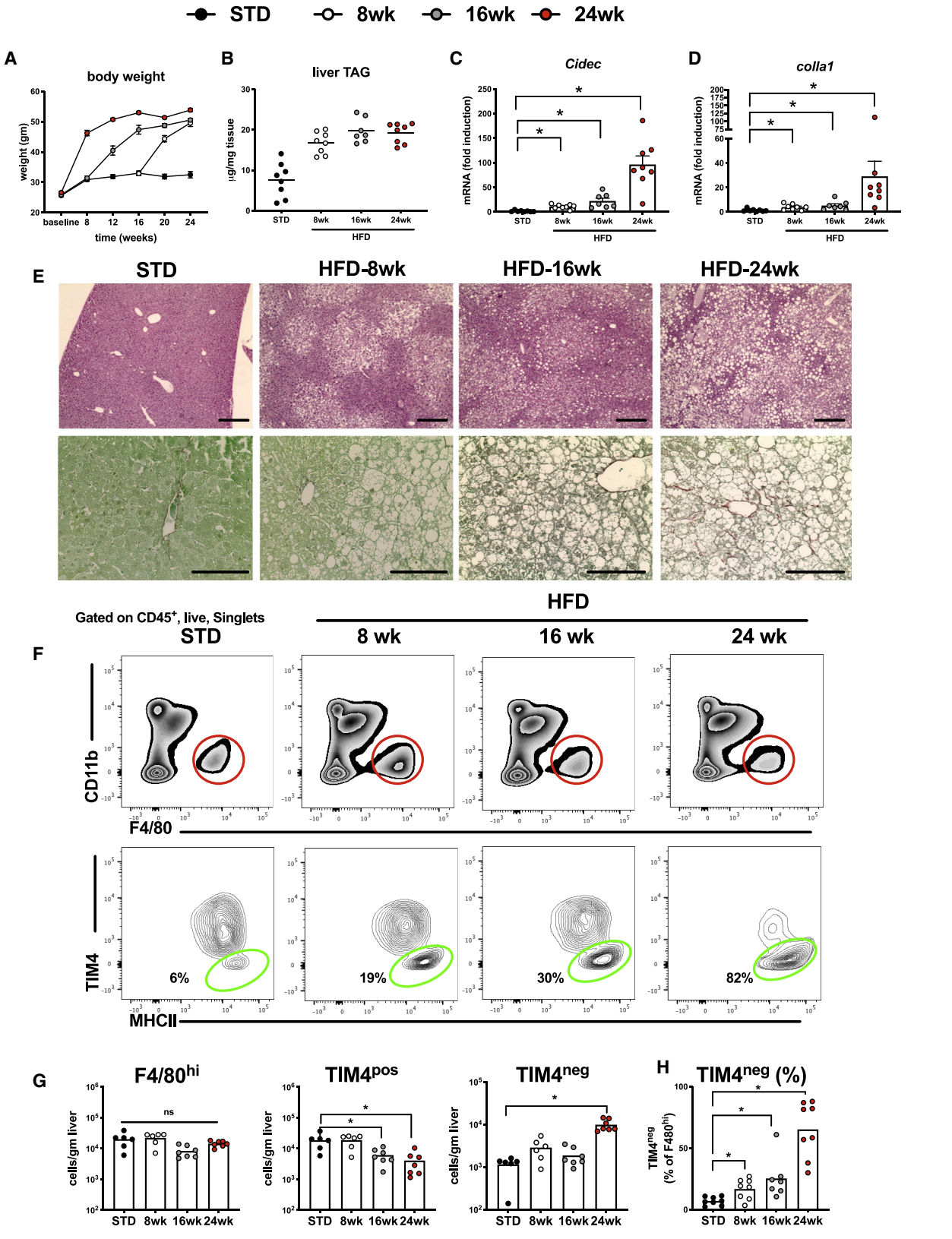


(legend on next page)

resolve because most studies have used general macrophage markers (CD11b, F4/80, CD68) and global depletion strategies to assess macrophage composition and function (Huang et al., 2010; Neyrinck et al., 2009; Reid et al., 2016; Stienstra et al., 2010; Tosello-Trampont et al., 2012). M1 and M2 nomenclature has also failed to describe diversity of macrophage phenotypes observed in obesity (Hill et al., 2018; Jaitin et al., 2019). The use of bulk and single-cell RNA-sequencing (scRNA-seq) has allowed for better resolution of macrophage heterogeneity in NAFLD/NASH (Krenkel et al., 2020; McGettigan et al., 2019). A recent study indicated the emergence of NASH-associated macrophages (NAMs), which were proposed to be KCs with high expression of *Trem2*, *Cd9*, and *Gpnmb* (Xiong et al., 2019). These macrophages appear similar to the *Trem2*/*Cd9*-expressing macrophages that accumulate in the adipose tissue with obesity and have been referred to as lipid-associated macrophages (LAMs) (Jaitin et al., 2019). However, it is unclear whether NAMs are newly recruited MdMs or represent a reprogramming of resident KCs. Moreover, the impact of these macrophages on the pathogenesis of NASH is also unknown.

The prevailing dogma is that KCs and total liver macrophage content increases during NASH progression. However, this notion has recently been challenged by a study conducted in a methionine-choline deficient (MCD) model of NASH (Devisscher et al., 2017). This study suggested that resident KCs may decrease during hepatic steatosis but are able to repopulate via recruitment of monocytes and KC proliferation after removal of the dietary stress. Whether similar events happen in models of NAFLD that more closely mimics the disease in people has not been determined.

In mice and humans with NASH macrophages often form clusters or aggregates in the liver, particularly in areas of macrovesicular steatosis. These cellular aggregates, known as hepatic crown-like structures (hCLSs), or lipogranulomas, are associated with the transition from simple steatosis to NASH (Ioannou et al., 2013, 2015, 2017; Kleiner et al., 2005; Tandra et al., 2011). The contribution of resident and/or recruited macrophages to the formation of these cell aggregates and whether these structures are detrimental or adaptive has been controversial (Itoh et al., 2013, 2017). The purpose of the present study was to investigate the dynamics of resident and recruited hepatic macrophage populations and to gain insight into their functional roles during the progression of NASH. Our data demonstrate that, in response to a high-fat, high-sucrose diet (HFD), the number of F4/80$^{hi}$ macrophages remains constant; however, the composition changes with a decrease in the number of resident KCs and an increase in MdMs within the "KC" gate (i.e., F480$^{hi}$/CD11b$^{int}$). MdMs were TIM4$^{neg}$ and could be divided into subsets in part based on based on expression of *Cx3cr1*, LAM markers (Gpnmb, CD63), and KC markers (VSIG4, CLEC4F) expression. MdMs expressing *Cx3cr1*/*Ccr2* localized to the hCLS and interacted other MdMs in these clusters. The expression of LAM markers was also highly enriched in the hCLS. Using *Ccr2* knockout (KO) mice, we provide evidence that MdMs preferentially accumulate in hCLSs, are required for hCLS formation, and appear to protect against adverse liver remodeling during NASH.

## RESULTS

### Mouse Model of NAFLD

To investigate the dynamics of macrophage populations in NAFLD, we first characterized the progression of obesity, insulin resistance, and liver steatosis in C57BL/6 mice fed a HFD. Male littermate mice were placed on a HFD in 8 week increments to allow comparison of metabolic and inflammatory phenotypes between mice of the same age. Using this approach, mice experienced a period of rapid weight gain during the first 8 weeks of a HFD followed by a period of slower weight gain from 8–24 weeks (Figure 1A). The final weight of mice on a HFD for 8, 16, or 24 weeks approached a similar peak. As expected, HFD feeding was associated with progressively worsening insulin resistance (Figure S1). Liver weight began to increase after 8 weeks on a HFD but accelerated between 16 and 24 weeks on a HFD (Figure S1). The concentration of triglycerides in liver tissue increased early and remained elevated throughout the study (Figure 1B). This was associated with increased expression of lipid droplet proteins and evidence of steatosis on histology (Figures 1C and 1E).

Histologic assessment demonstrated that liver steatosis occurred in a regional pattern (Figure 1E). Mice fed a HFD for 8 weeks exhibited pericentral steatosis, similar to what has been described for early stages of NAFLD in humans (Brunt et al., 1999). With increasing time on the diet, the amount of macrovesicular steatosis increased and steatosis began to involve the periportal region of the liver. In conjunction with worsening steatosis, markers of liver fibrosis also began to increase by 24 weeks of a HFD (Figure 1D). Picrosirius red staining (PRS) of liver sections confirmed increasing interstitial "chicken-wire" fibrosis (Figure 1E). Thus, HFD feeding leads to weight gain, insulin resistance, liver steatosis, and liver fibrosis, which are hallmarks of the metabolic syndrome and early NASH in humans.

**Figure 1. Accumulation of TIM4$^{neg}$ Macrophages in a Mouse Model of NASH**

(A) Body weight of C57BL/6 male mice fed a HFD for the indicated time.

(B–D) Liver triglyceride (B) and mRNA markers of steatosis (C) and fibrosis (D) were quantified.

(E) H&E (top panels) and picrosirius red (bottom panels) from liver tissue.

(F) Flow-cytometry plots are shown for CD45$^{+}$, live, singlets (top panels). Representative plots of F4/80$^{hi}$ cells (red gate) were analyzed for expression of TIM4 (bottom panels).

(G) Quantification of flow data per gram of liver tissue.

(H) Percentage of F4/80$^{hi}$ cells that are TIM4$^{neg}$ over course of HFD feeding.

In (A), each dot represents the mean ± SEM and in (B)–(D). In (G), each dot represents a single mouse, and the mean is shown (n = 7–8 mice/group). The data represent the results of one independent experiment with n = 7–8 mice per group. *$p < 0.05$ for HFD versus STD. Scale bars, 250 μm

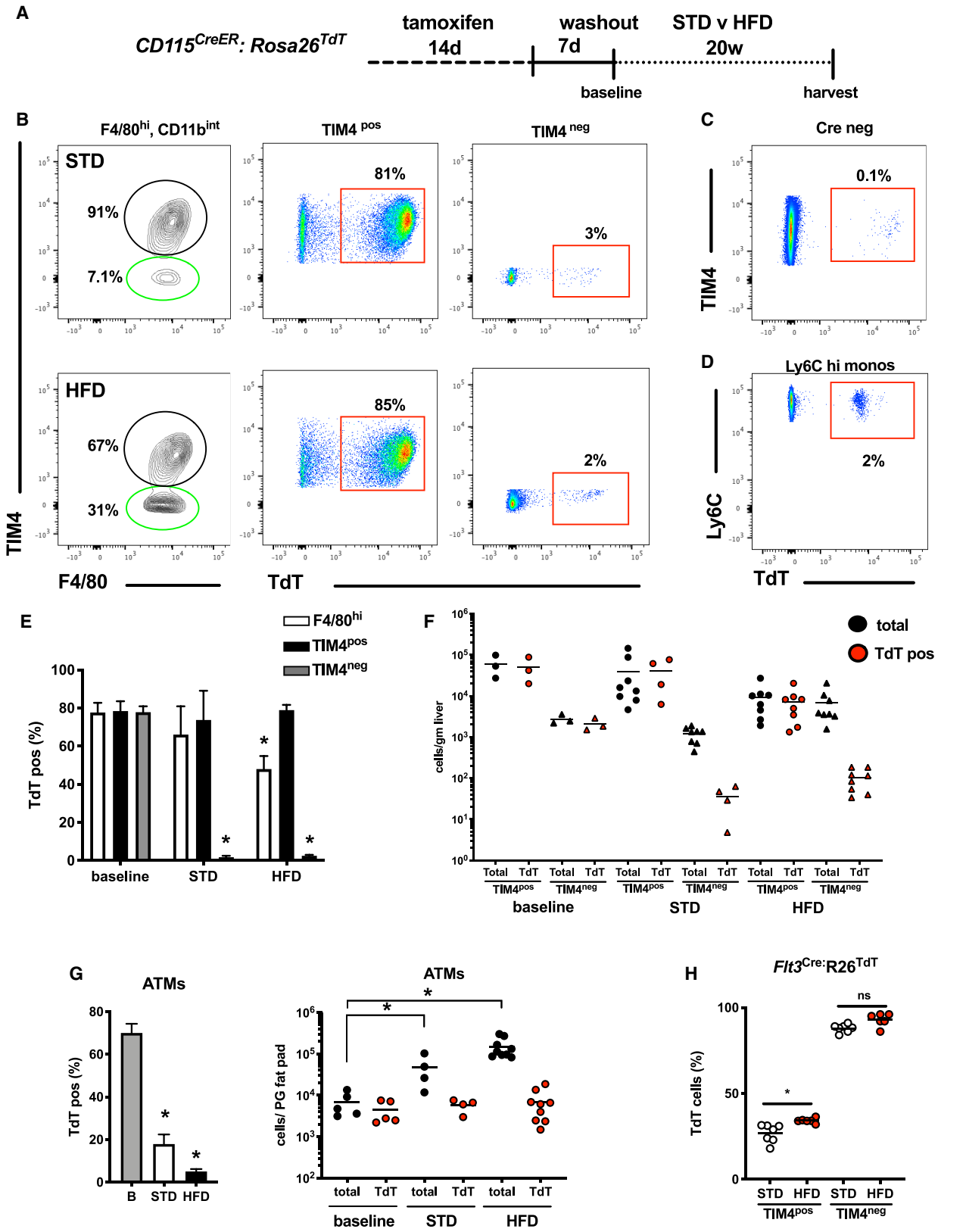


*(legend on next page)*

### Macrophage Dynamics with NAFLD Progression

To understand the dynamics of macrophage biology during the progression of NAFLD, we analyzed myeloid cell populations using flow cytometry, immunofluorescence (IF), and mRNA from the kinetic HFD study. We first assessed CD11b and F4/80 expression in CD45$^{pos}$ cells based on prior data that resident KCs are F4/80$^{hi}$, CD11b$^{int}$, whereas the infiltrating monocyte-derived cells are CD11b$^{hi}$, F4/80$^{int}$ (Schulz et al., 2012). The number of CD11b$^{hi}$ cells increased with time on diet, whereas the F4/80$^{hi}$ cell number remained relatively constant (Figure 1F). Further assessment of the CD11b$^{hi}$ population revealed that this cell gate consists of several leukocyte populations including Ly6C$^{hi}$ monocytes, Ly6C$^{hi}$/MHCII$^{hi}$ monocytes, Ly6C$^{lo}$ monocytes, eosinophils, neutrophils, and conventional dendritic cells type 2 (cDC2; Figure S1). The number of F4/80$^{hi}$ cells did not significantly change over time; however, there was a dramatic increase in the number of TIM4$^{neg}$ macrophages in this gate (Figures 1F and 1G). Mice fed a standard diet (STD) had a low percentage of F4/80$^{hi}$, TIM4$^{neg}$ cells (3%–11%), likely representing liver capsular macrophages (Sierro et al., 2017), whereas by 24 weeks of a HFD nearly 80% of the F4/80$^{hi}$ cells were TIM4$^{neg}$ (Figure 1G). Although F4/80$^{hi}$, TIM4$^{neg}$ cells began to appear by 8 weeks of a HFD, the number of these cells increased dramatically around 16 weeks of HFD feeding and accompanied a significant decrease in the number of TIM4$^{pos}$ KCs. At baseline TIM4 is expressed selectively on mature KCs in the liver and is absent from MdMs or recently differentiated monocyte-derived KCs (Mo-KCs); therefore, these data suggested that monocyte-derived cells were entering the F4/80$^{hi}$ "KC" gate during NASH (Beattie et al., 2016; Scott et al., 2016).

To confirm that the changes in macrophage composition detected by flow cytometry were reflective of macrophage changes in the tissue, we performed mRNA and IF analysis on liver tissue. At the mRNA level, *Adgre1* (F4/80) expression remained stable throughout the time course of a HFD until 24 weeks when it began to increase. In contrast, *Timd4* (TIM4) expression decreased by the 24 week time point leading a substantial reduction in the ratio of *Timd4* to *Adgre1* (Figure S2). Similar findings were also seen with tissue imaging. CLEC4F staining co-localized with F4/80$^{pos}$ and TIM4$^{pos}$ cells in STD-fed mice confirming that KCs are the primary F4/80$^{hi}$ cells in the liver at baseline (Figure S2). After 24 weeks of a HFD, TIM4$^{pos}$ and CLEC4F$^{pos}$ cells were decreased in the liver tissue and F4/80$^{hi}$ cells lacking these KC markers were present. CLEC4F and TIM4 expression frequently co-localized in HFD-fed mice suggesting that Mo-KCs (CLEC4F$^{pos}$, TIM4$^{neg}$) were rare at this time point (Figure S2). In summary, a HFD induces a shift in the composition of F4/80$^{hi}$, CD11b$^{int}$ hepatic macrophages characterized by a decrease TIM4$^{pos}$ KCs and a concomitant increase in the number of TIM4$^{neg}$ macrophages.

### TIM4$^{neg}$ Macrophages Are Monocyte Derived

The finding that F4/80$^{hi}$, TIM4$^{neg}$ macrophages accumulate with HFD feeding suggested that monocytes were entering the liver and differentiating into hepatic macrophages or Mo-KCs. However, the possibility that KCs might downregulate TIM4 expression in response to lipid stress could not be excluded. To evaluate these possibilities, we utilized complimentary lineage tracing and fate-mapping approaches. First, we employed CD115$^{CreER}$Rosa26$^{TdTomato\ (TdT)}$ mice, which allow for tamoxifen-inducible labeling of CD115 (CSFR1)-expressing cells. For these experiments, mice were fed tamoxifen chow for 2 weeks to activate the reporter in monocytes and macrophages (Figure 2A). Subsequently, the mice were placed on a chow diet for 7 days for label washout (Bajpai et al., 2019)and a subset of mice was harvested to assess the labeling efficiency. Approximately 80% of mature KCs were labeled using this protocol, which was in stark contrast to Ly6C$^{hi}$ monocytes where <5% of the cells remained TdT positive after washout (Figure 2B).

To assess influx of unlabeled monocyte-derived cells and to evaluate the persistence of KCs, mice were placed on a STD or HFD for 20 weeks after the tamoxifen induction. Consistent with the long lifespan of resident KCs, the number of TdT-labeled F4/80$^{hi}$, TIM4$^{pos}$ cells remained constant in number and percentage over time in STD-fed mice (Figures 2B, 2E, and 2F). Although there were a small number of F4/80$^{hi}$,TIM4$^{neg}$ cells in the liver in STD-fed mice, nearly all of these cells were TdT negative after 20 weeks indicating they had been replaced by unlabeled cells. With HFD feeding, the percentage of F4/80$^{hi}$ cells containing TdT label decreased , consistent with the influx of unlabeled monocyte-derived cells. The percentage of TdT$^{pos}$,TIM4$^{pos}$ KCs remained constant with a HFD despite a decrease in the total number of TIM4$^{pos}$ cells (Figures 2E and 2F). The F4/80$^{hi}$, TIM4$^{neg}$ macrophages lacked expression of the reporter indicating that the decrease in F4/80$^{hi}$,TdT$^{pos}$ cells resulted from infiltration of

**Figure 2. TIM4$^{neg}$ Macrophages in the Kupffer Cell Gate Are Monocyte Derived**

(A) CD115-CreER mice were crossed with Rosa26$^{TdT}$ mice to for fate mapping. Male mice were fed tamoxifen (2 weeks) to induce labeling. After a 1 week washout period, the mice were started on STD/HFD.

(B) Representative flow plots are shown for CD45$^{+}$, singlet, live cells that were F4/80$^{hi}$, CD11b$^{int}$. TIM4$^{pos}$ (black) and TIM4$^{neg}$ (green) macrophages are shown, and TdT expression was assessed (red).

(C) F4/80$^{hi}$ macrophages from Cre negative Rosa26$^{TdT}$ treated with tamoxifen for 2 weeks.

(D) TdT label present in Ly6C$^{hi}$ monocytes at 20 weeks.

(E) Percentage of TdT-labeled cells in the total F4/80$^{hi}$ gate (white bars); F4/80$^{hi}$,TIM4$^{pos}$ (black bars); and F4/80$^{hi}$,TIM4$^{neg}$ (gray bars) at baseline or following STD/HFD.

(F) Quantitation of total (black dots) or TdT-labeled (red dots) TIM4$^{pos}$ and TIM4$^{neg}$ F4/80$^{hi}$ macrophages in the liver following the indicated diet interventions.

(G) The percentage of labeled ATMs (CD11b$^{hi}$, F4/80$^{hi}$, CD64$^{hi}$) is shown in the left panel with the total number of labeled and unlabeled macrophages shown in the right panel.

(H) *Flt3*-Cre;Rosa26$^{TdT}$ mice were fed a STD or HFD and percentage of labeled TIM4$^{pos}$ and TIM4$^{neg}$ macrophages cells was determined by flow cytometry.

All dots represent data from one mouse with the mean shown in the bar. The bar graphs represent the mean of the group. The data represent the results of three independent experiments with n = 3–8 mice per groups. *p < 0.05.

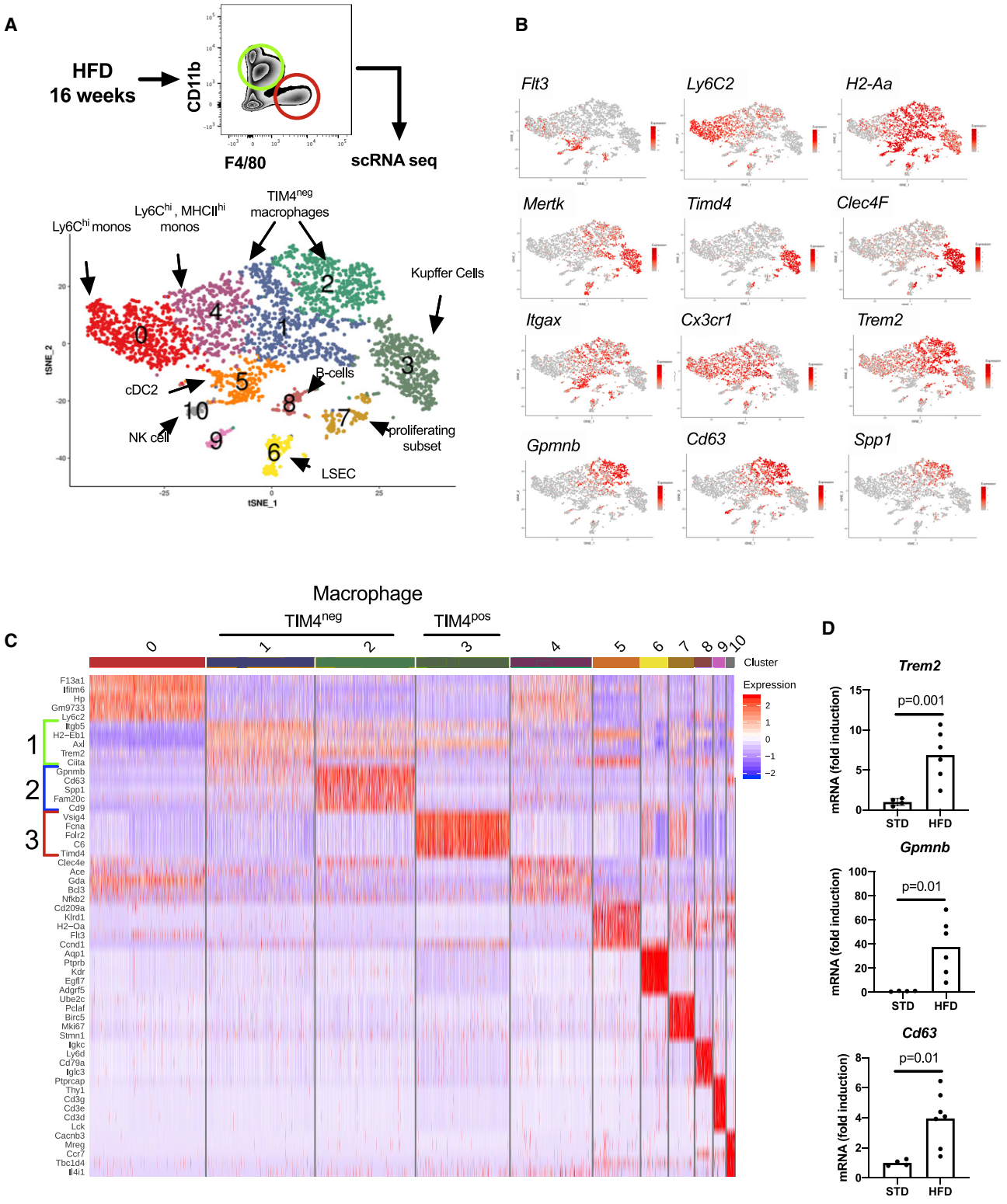


**Figure 3. Transcriptional Profiling of Hepatic Macrophages during NASH**

(A) CD45$^{+}$, live, singlet cells were prepared and pooled together from 3 individual mice fed HFD for 16 weeks and the hepatic non-parenchymal cells were flow sorted into CD11b$^{hi}$, F4/80$^{int}$ (green gate) and F4/80$^{hi}$, CD11b$^{int}$ (red gate) populations with removal of PMNs and eosinophils form the CD11b$^{hi}$ gate. The

*(legend continued on next page)*

F4/80$^{hi}$, TIM4$^{neg}$ cells that were unlabeled (i.e., monocyte-derived cells that appeared after the initial labeling). Together these findings argue that the TIM4$^{neg}$ macrophages develop *de novo* from monocytes and not via loss of TIM4 expression from resident KCs. However, we cannot exclude that a TIM4$^{neg}$ precursor cell from the liver could also give rise to these macrophages. The minimal dilution of TIM4$^{pos}$, TdT$^{pos}$ cells by unlabeled cells during HFD feeding also argues that the majority of the newly recruited MdMs do not become mature TIM4$^{pos}$ KCs at this stage of disease.

To ensure that our flow-cytometry data were reflective of the tissue, we also performed IF with antibodies to F4/80, CLEC4F, and TIM4 in the CD115$^{CreER}$Rosa26$^{TdT}$ system. Nearly all of the TIM4-expressing cells contained the TdT reporter (Figure S3). However, F4/80$^{pos}$ cells that lacked TdT expression could be readily identified in the livers of HFD-fed mice (Figure S3). Although the majority of CLEC4F-expressing cells were also TdT$^{pos}$ at this time point, there were some cells lacking TdT expression, suggesting they were Mo-KCs. Although it is possible that some Mo-KCs could have upregulated TIM4 during the course of these experiments, and thus would not be discernable from Em-KCs in this experimental model, it is less likely as TIM4 expression in Mo-KCs requires several weeks to months (Scott et al., 2016).

We also analyzed adipose tissue macrophage (ATM) persistence using these same reporter mice. Similar to the liver, ~70% of the resident ATMs were labeled with TdT following tamoxifen feeding. Distinct from what was observed in the liver, the number of ATMs increased with age in both STD- and HFD-fed mice, and after 20 weeks the majority of these macrophages lacked TdT expression (Figure 2G). Mice fed a HFD had a greater increase in the number of ATMs over time, and the percentage of TdT$^{pos}$ macrophages was even further diminished. These findings indicate that most of the ATMs that arise from HFD exposure do not come from the initial resident population, which remained constant in number during this experiment. Thus, the influx of monocyte-derived cells and maintenance of resident macrophages with obesity is different in adipose tissue compared to liver.

As a complementary method to assess the origin of hepatic macrophages in the KC and TIM4$^{neg}$ pool, we employed a linage tracing approach using *Flt3*-Cre; *Rosa26*$^{TdT}$ (Epelman et al., 2014). Using this system, cells that arise from definitive hematopoiesis are labeled with TdT. At baseline, ~25% of the TIM4$^{pos}$ KCs were labeled with the reporter, which is consistent with prior reports (Gomez Perdiguero et al., 2015; Scott et al., 2016). In the mice that were fed a STD for 20 weeks, the number of labeled KCs was similar to baseline (Figure 2H). In mice fed a HFD for 20 weeks, the number of TdT$^{pos}$ cells in the TIM4$^{pos}$ KC pool was significantly increased compared to a STD, but the difference was modest (34% versus 27%, p = 0.007). Greater than 95% of the TIM4$^{neg}$ macrophages were TdT$^{pos}$, confirming these cells arise from definitive hematopoiesis. In concert, our data from these two reporter systems confirm that the F4/80$^{hi}$, TIM4$^{neg}$ macrophages that accumulate in liver with a HFD are of bone-marrow origin and rarely differentiate into fully mature TIM4-expressing KCs at this stage of disease.

## Defining Macrophage Heterogeneity during NASH

The increase in F4/80$^{hi}$, TIM4$^{neg}$ MdMs suggested that monocytes were entering the liver to fill the partially opened KC niche or as a response to liver damage or both. To investigate the heterogeneity of these cells and to gain insight into their biologic function, we performed scRNA-seq on CD11b$^{hi}$, F4/80$^{int}$ and CD11b$^{int}$, F4/80$^{hi}$ cells after 16 weeks of HFD feeding. The data revealed several distinct clusters of myeloid cells including monocytes (cluster 0; *Ly6C2*, *Ccr2*, *Itgam*/CD11b), dendritic cells (cluster5; *Flt3*, *Zbtb46*, *MHCII*, *Itgax*/CD11c), and macrophages (clusters 1–3; *MerTK*, *FcGR1a*/CD64; Figures 3A and 3B). Cluster 4 consisted of cells with decreasing Ly6C and increasing MHCII/CD11c suggestive of the transitional monocytes that appear with KC depletion in the normal liver (Figures 3A and 3B; Bonnardel et al., 2019). Within the macrophage populations, KCs were represented by cluster 3 (*Timd4*, *Clec4F*, *Marco*, *Cd163*), whereas clusters 1 and 2 contained TIM4$^{neg}$ MdMs (Figures 3B and 3C). The top 5 unique genes for each cluster are shown as a heatmap in Figure 3C. Both cluster 1 and 2 had high expression of *Trem2*, a gene associated with LAMs/NAMs (Jaitin et al., 2019; Xiong et al., 2019), whereas the expression of this marker was low in KCs. There was also a progressive increase in gene expression of other LAM/NAM markers such as *Cd9*, *Cd63*, and *Gpmnb* from cluster 1 to cluster 2 macrophages. KCs did not express these markers to a significant extent. Thus, the previously described NAMs appear to represent a newly recruited MdM population rather an alternative activation state of KCs (Figure 3C). Although we did not have scRNA-seq of liver macrophages from a STD for comparison, we did perform qPCR on mouse livers at baseline and following HFD feeding and observed increased expression of macrophage markers associated with cluster 1 and 2 (*Trem2*, *Gpnmb*, and *Cd63*) with a HFD (Figure 3D).

The TIM4$^{neg}$ MdMs from cluster 1 had higher expression of the monocyte markers *Cx3cr1* and *Ccr2*, whereas these markers were lower in cluster 2 and absent from KCs. Thus, with a HFD the F4/80$^{hi}$ KC gate noted on flow cytometry would be anticipated to contain not only resident KCs but at least two distinct *Trem2* positive MdM populations. Cluster 1 macrophages appear to be a transitional macrophage subset with higher expression of *Cx3Cr1*/*Ccr2* and lower expression of *Cd63*, *Cd9*, and *Gpmnb*, whereas cluster 2 cells have lower expression

remaining cells were pooled 1:1 to create the hepatic macrophage/monocyte subsets and the sample was subjected to 10× scRNA-seq. The cluster-based t-SNE plot of the cell clusters is shown.

(B) Expression of the indicated genes as shown using t-SNE visualization.

(C) K means clustering analysis of the top 5 genes from each leukocyte population. TIM4$^{neg}$ macrophages are represented by clusters 1 (green) and 2 (blue), whereas cluster 3 represents TIM4$^{pos}$ KCs (red).

(D) mRNA expression of genes associated with TIM4$^{neg}$ macrophages in liver tissue from mice fed a STD or HFD for 16 weeks. Bars represent the means, and each dot represents a single mouse. The data represent the results of one independent experiment with n = 4–5 mice per groups. The p values are shown.

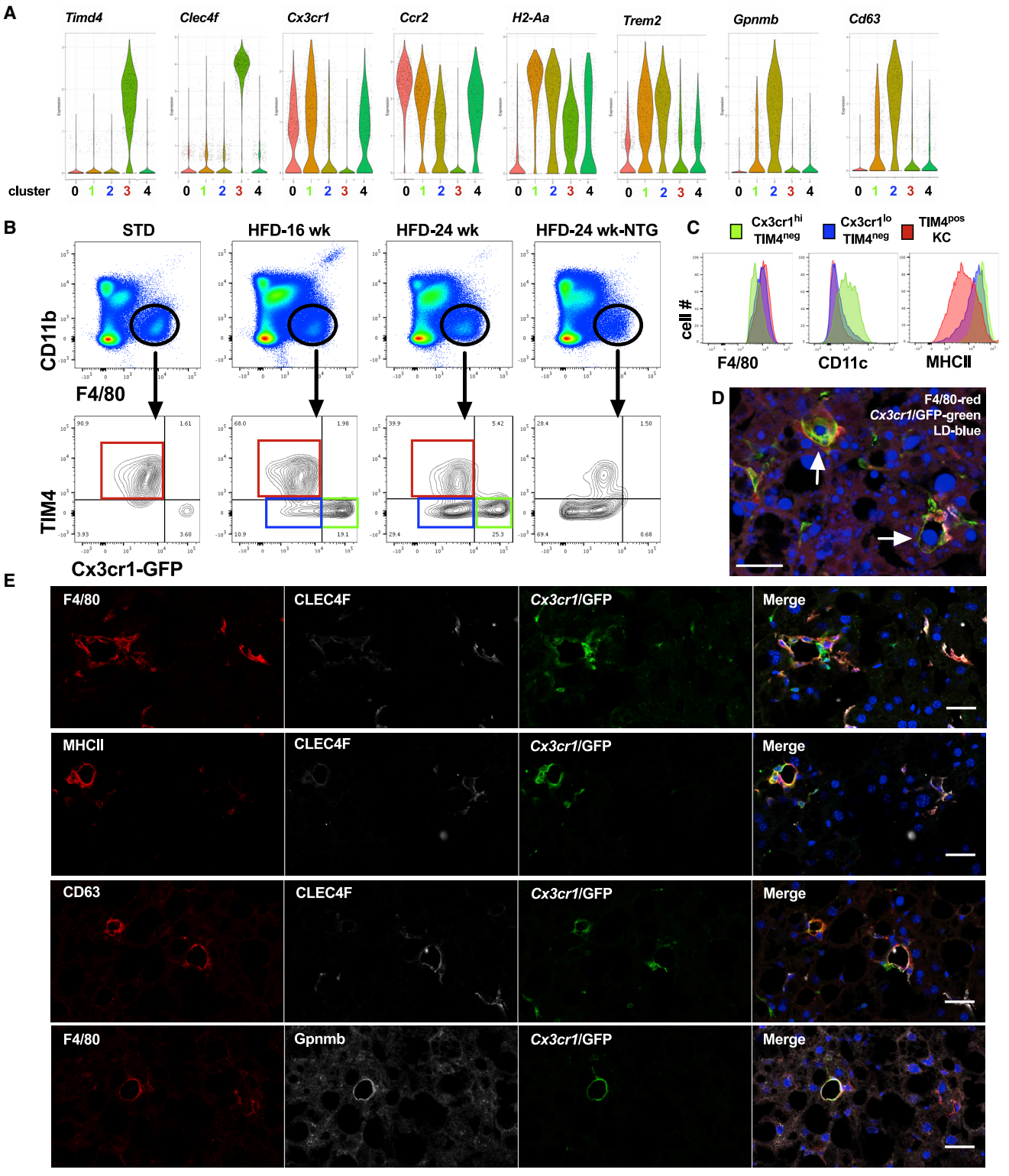


**Figure 4. TIM4$^{neg}$ Macrophage Subsets Accumulate with NASH and Form Macrophage Aggregates in the Liver**

(A) Violin plots of macrophage markers in monocyte/macrophage clusters where the macrophages are clusters 1: *Cx3cr1*$^{hi}$,*Timd4*$^{neg}$ (green), 2: *Cx3cr1*$^{lo}$,-*Timd4*$^{neg}$ (blue), 3: KCs (red).

(B) F4/80$^{hi}$, CD11b$^{int}$ cells (too panels) assessing TIM4 and *Cx3cr1* expression (bottom panels) from indicated conditions. The boxes indicate cells corresponding to the clusters shown above.

*(legend continued on next page)*

of *Cx3Cr1*/*Ccr2* and higher expression of *Cd63*, *Cd9*, *Gpmnb*, and *Spp1*. Importantly, *GATA6* was not expressed in either MdM population indicating that they were unlikely to originate from the large subset of peritoneal macrophages. Recently, macrophages with a gene-expression profile matching our cluster 2 cells were described as hepatic LAMs (Remmerie et al., 2020). Therefore, to maintain consistency with previously utilized nomenclature, we will refer to the *Cx3cr1*$^{hi}$, TIM4$^{neg}$ cells and *Cx3cr1*$^{lo}$, TIM4$^{neg}$ cells as hepatic C-LAMs and LAMs, respectively. At the 16 week time point, very few TIM4$^{neg}$, CLEC4F$^{pos}$ Mo-KCs were observed in the scRNA-seq analysis.

### MdMs and Aggregate Formation in the NASH

To validate our scRNA-seq data, we leveraged the differential expression *Cx3cr1*, LAM-associated genes (*Gpmnb*, and *Cd63*), and classic KC genes (*Timd4*, *Clec4F*) in the macrophage clusters 1, 2, and 3 (Figure 4A). Using *Cx3cr1*-GFP reporter mice, we analyzed the composition of TIM4$^{neg}$ macrophages from mice fed a STD or HFD for 16 or 24 weeks via flow cytometry. As expected, KCs did not express the reporter at baseline or following HFD. Although a slight shift was observed in the green channel for KCs it was similar in STD, HFD, and GFP$^{neg}$ littermates indicating that this signal was the result of autofluorescence (Figure 4B). Consistent with the scRNA-seq analysis, the F4/80$^{hi}$, TIM4$^{neg}$ cells could be divided into reporter high and reporter low subsets (Figure 4B). We observed that with more time on a HFD, the number of TIM4$^{pos}$ KCs decreased, and this was associated with a further increase in TIM4$^{neg}$ macrophages. Notably, a more pronounced expansion of TIM4$^{neg}$, *Cx3Cr1*$^{lo}$ cells was observed as TIM4$^{pos}$ KCs decreased, suggesting some of these cells could be entering the niche vacated by loss of resident macrophages (i.e., Mo-KCs). Flow-cytometry data demonstrated that TIM4$^{neg}$, *Cx3cr1*$^{hi}$ macrophages had slightly lower expression of F4/80, higher expression of MHCII, and intermediate expression of CD11c, a profile associated with transitional macrophages (Bonnardel et al., 2019). TIM4$^{neg}$ macrophages continued to have high expression of MHCII irrespective of *Cx3Cr1* expression level; however, CD11c expression was lower in *Cx3cr1*$^{lo}$ macrophages (Figure 4C). The TIM4$^{neg}$, *Cx3Cr1*$^{hi}$ macrophages also tended to be smaller and less granular than TIM4$^{neg}$, *Cx3Cr1*$^{lo}$ cells, further suggesting they represent early MdMs (Figure S4A). Together these data confirm the presence *Cx3cr1*$^{hi}$ and *Cx3cr1*$^{lo}$ TIM4$^{neg}$ macrophages that accumulate with the development of NASH.

To further validate these macrophage populations in tissue and to assess their localization during the progression of NAFLD, we performed IF imaging of livers from *Cx3cr1*$^{gfp/wt}$ mice. In mice fed a STD diet, GFP-expressing cells were rarely seen in the liver parenchyma/sinusoids where F4/80, CLEC4F double-positive cells predominated (Figure S4C). GFP$^{pos}$ cells were evident in the walls of the larger portal blood vessels and could also be observed under the liver capsule (Sierro et al., 2017; Yona et al., 2013). After HFD feeding, GFP-expressing cells were abundant in the hepatic parenchyma, and many of these cells also expressed F4/80, albeit less bright than KCs, and generally had low expression of markers such as CLEC4F (Figure 4E). GFP$^{pos}$ cells were most often located in macrophage aggregates in association with F4/80$^{hi}$, CLEC4F$^{lo}$, GFP$^{neg}$ macrophages (Figure 4C). The morphology of GFP$^{pos}$ cells varied from a small round shape suggestive of monocytes to an elongated form that was present in the aggregates (Figure 4E).

Based on the differential expression of MHCII between C-LAMs/LAMs and KCs by scRNA-seq and flow cytometry, we assessed expression of this marker in the tissue. MHCII expression was higher in hCLSs and macrophage aggregates compared to CLEC4F$^{pos}$ KCs (Figure 4E). The LAM/C-LAM marker CD63 was also evaluated by IF. With the STD diet, CD63 staining was not observed in the liver tissue (Figure S4). However, with liver steatosis, CD63 positive cells were abundant and were predominantly located in macrophage aggregates/hCLS. CD63 staining was also observed in some GFP$^{pos}$ cells and rarely observed in CLEC4F-expressing cells (Figure 4E). A similar pattern was seen with staining for the LAM marker Gpnmb, where no positive cells were observed with a STD, but with a HFD a subset of macrophages expressing Gpnmb could be identified within macrophage aggregates/hCLS (Figure 4E). These data validate scRNA-seq analysis and reveal that C-LAMs and LAMs preferentially localize in macrophage aggregates in areas of macrovesicular steatosis (Figure 4D).

The association of MdMs with cell aggregates and hCLSs was reminiscent of macrophage structures that form in the adipose tissue during obesity (Hill et al., 2018; Jaitin et al., 2019). We therefore compared bulk RNA-seq data from TIM4$^{neg}$, *Cx3Cr1*$^{hi}$ macrophages to ATMs from HFD-fed mice. NASH KCs and STD KCs were used as a comparator (Figure S5). Consistent with the scRNA-seq data, the gene-expression profile of the incoming TIM4$^{neg}$, *Cx3Cr1*$^{hi}$ macrophages was enriched for genes involved in lipid metabolism, matrix remodeling, and cell adhesion (Figure S5). Comparing the expression of previously published LAM markers (Jaitin et al., 2019) in TIM4$^{neg}$, *Cx3Cr1*$^{hi}$ liver macrophages and ATMs revealed strong similarities with increased expression of *Trem2*, *Spp1*, *Cd63*, *Cd9*, and *Gpnmb*. However, there were also several liver niche-specific genes that distinguished liver macrophages from ATMs including expression of *Id3*, *Nr1h3* (LXR), fatty acid binding protein 7 (*Fabp7*), and *Clec1b*/CLEC2 (Figure S5). TIM4$^{neg}$, *Cx3Cr1*$^{hi}$ macrophages also had intermediate expression of *Clec4f* and *Vsig4*, but low expression of *Timd4*, *Cd163*, and *Marco*. Together, these findings suggest that, as monocytes enter the liver, they receive cues from the liver niche that drives expression of KC markers and/or respond to inflammatory/lipid stimuli, which induce expression of LAM genes. Based on these data, it is possible that the transitional TIM4$^{neg}$, *Cx3Cr1*$^{hi}$ macrophages represent cells transitioning to LAMs and/or Mo-KCs. TIM4$^{neg}$, *Cx3Cr1*$^{hi}$ macrophages also share expression of a subset of genes associated with scar-associated macrophages (SAMs) from human

(C) Histogram of F4/80, CD11c, and MHCII on the indicated macrophage populations.
(D) IF analysis of F4/80 and *Cx3cr1*-GFP with lipid stain monodansylpentane (MDH). Arrows indicate aggregates around lipid droplets.
(E) Images of macrophage aggregates using IF to assess expression of markers identified in (A), including CLEC4F, MHCII, CD63, and Gpnmb.
The results are from three independent experiments n = 4–8 mice/group. Scale bars, 30 μm.

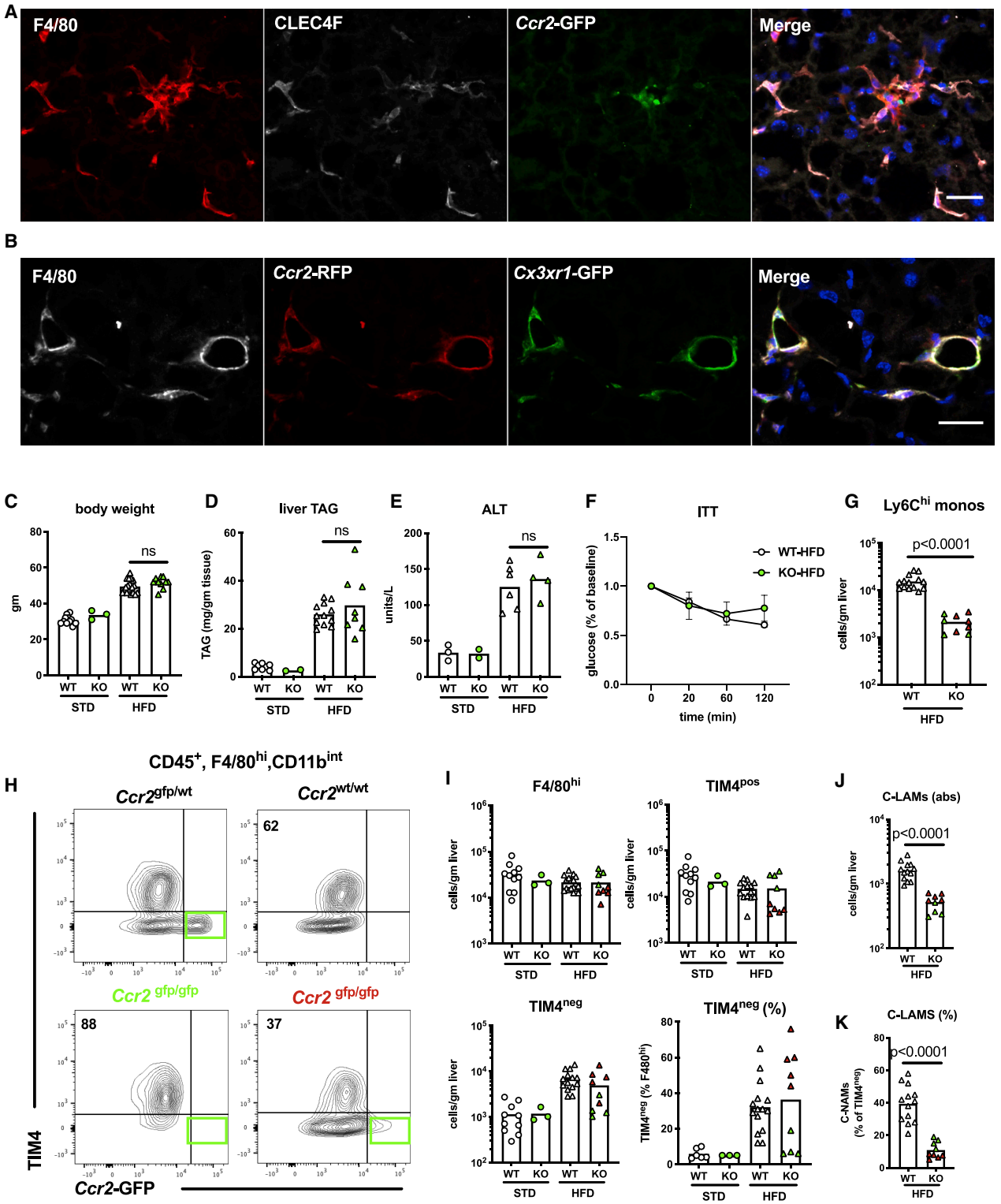


**Figure 5. Loss of Ccr2 Prevents Accumulation of C-LAMs with NAFLD**

(A) Image of a macrophage aggregate stained for F4/80, CLEC4F, and *Ccr2*-GFP.

(B) Image of macrophage clusters from mice co-expressing *Ccr2*-RFP and *Cx3cr1*-GFP.

(C–F) Body weight (C), liver TAG (D), and serum ALT (E) from WT and KO mice fed a STD/HFD for 20 weeks. (F) ITT from WT or KO mice fed a HFD.

*(legend continued on next page)*

cirrhosis (*Cd9*, *Cd63*, *Lgals3*, *Spp1*) further suggesting they may be involved in tissue remodeling (Figure S5).

## CCR2 Is Required for Accumulation of C-LAMs in NASH

CCR2 is chemokine receptor expressed on circulating monocytes that is required for their efficient recruitment to tissues. *Ccr2*-deficient mice have reduced numbers of circulating Ly6C$^{hi}$ monocytes and impaired monocyte entry into tissues. However, resident macrophage populations are largely intact in these mice. As TIM4$^{neg}$ macrophages are monocyte derived, we sought to evaluate the impact of *Ccr2* loss of function on these macrophage populations during NASH. *Ccr2*-GFP knockin reporter mice were bred to generate mice that were wild-type (WT), heterozygous, or KO for *Ccr2*. We first confirmed that *Ccr2*-expressing cells localized to macrophage aggregates and that *Ccr2* and *Cx3Cr1* expression identifies the same cell population using *Cx3cr1*-GFP, *Ccr2*-RFP double reporter mice (Figures 5A and 5B). To address the impact of *Ccr2* deficiency on liver phenotypes, mice were placed on a HFD for 20 weeks. Despite conflicting reports in the literature regarding the impact of *Ccr2* deficiency on obesity/insulin resistance, we observed similar weight gain, insulin tolerance, liver size, and liver TAG in WT and *Ccr2* KO animals (Figures 5C–5F). As anticipated, the number of Ly6C$^{hi}$ monocytes in the liver was dramatically reduced, and small changes in the DC number were observed (Figure 5G; Figure S6). Analysis of the F4/80$^{hi}$, TIM4$^{neg}$ macrophages in *Ccr2*$^{gfp/wt}$ was similar to *Cx3cr1*-GFP mice and revealed both *Ccr2*$^{hi}$ and *Ccr2*$^{lo}$ subsets (Figure 5H). *Ccr2* KO mice fed a HFD on the other hand displayed two distinct patterns of macrophage accumulation. In 4/9 (44%) of mice, there was a marked reduction in the total number of TIM4$^{neg}$ macrophages (Figures 5H–5K, green symbols). However, in 5/9 (56%) of the *Ccr2* KO mice, Tim4$^{neg}$ macrophages were present in the liver to a similar degree as WT mice (Figures 5H–5K, red symbols). However, C-LAMs were reduced in number and percentage in all *Ccr2* KO mice (Figures 5J and 5K). The number of TIM4$^{neg}$ macrophages was greatest in *Ccr2* KO mice with more depletion of TIM4$^{pos}$ KCs, suggesting some of these cells may have emerged to fill a depleted KC niche. Thus, TIM4$^{neg}$ macrophages can still appear in the livers of *Ccr2* KO mice, yet C-LAMs are dramatically decreased.

## C-LAMs Are Required for the Formation of Macrophage Aggregates in NASH

The consistent reduction in C-LAMs in *Ccr2* KO mice allowed us to evaluate the role of this transitional population of macrophages in the formation of aggregates and acquisition of the LAM phenotype. To assess macrophage distribution and aggregate formation, liver tissue from HFD-fed WT and KO mice was stained for GFP and F4/80, and the number of macrophage aggregates and aggregates containing GFP-expressing cells was quantified (Figure 6A). In mice with intact *Ccr2*, cell aggregates were abundant, and the vast majority contained *Ccr2*$^{pos}$ C-LAMs. In contrast, mice lacking *Ccr2* had a significant decrease in the number and size of macrophage aggregates, and this was true even though the total number of F4/80$^{hi}$ cells was similar (Figures 6A and 6B). In addition, this pattern was consistent in all KO mice regardless of the number of TIM4$^{neg}$ cells. Although rare, when aggregates were present in *Ccr2* KO mice, at least one *Ccr2*-GFP positive cell was present (Figure 6B). Together these findings support the concept that C-LAMs not only accumulate in macrophage aggregates but also play a key role in their formation.

To further dissect the impact of *Ccr2* deficiency on macrophage phenotypes in the liver tissue, we stained the tissue with other markers of C-LAMs/LAMs including CD63 and Gpmnb. As seen in *Cx3Cr1*-GFP mice, CD63 and Gpmnb-expressing cells again localized to macrophage aggregates/hCLSs. In contrast, the CD63 and Gpmnb-expressing cells were rare in *Ccr2* KO mice and no longer localized in aggregates (Figures 6C and 6D). Thus, loss of *Ccr2* alters the number and organization of hepatic C-LAMs and LAMs in the liver tissue.

To determine whether C-LAM-like cells were present in the human liver, we performed IF on human liver samples from obese patients undergoing bariatric surgery. Macrophages were detected using antibodies to CD68 and CCR2. Similar to mouse tissues, we were able to observe cell aggregates in the human liver and these aggregates consisted of both CCR2$^{pos}$ and CD68$^{pos}$ cells (Figure 6E). In addition, CCR2$^{pos}$ cells frequently interacted with other macrophages to form cell aggregates. Together these findings indicate that CCR2$^{pos}$ cells that resemble C-LAMs are present in livers of humans with NAFLD.

Macrophage aggregation and hCLS formation have been associated with tissue fibrosis in NASH. Moreover, CCR2 antagonists are currently being considered as an anti-fibrotic strategy for patients with NASH (Lefere et al., 2020). Thus, we hypothesized that impaired assembly of C-LAMs and LAMs into macrophage aggregates would influence liver fibrosis. Surprisingly, we observed a significant increase in liver fibrosis in the *Ccr2* KO mice. Most of the fibrosis was noted in regions of abundant macrovesicular steatosis, where aggregates and hCLSs tend to form (Figure 6F). These observations suggest that C-LAMs and LAMs in macrophage aggregates may play a protective role against NASH fibrosis potentially via the containment and/or clearance of dead cells or excess toxic lipids.

## Ccr2 KO Disrupts hCLS Formation and Promotes Fibrosis in a NASH Fibrosis Model

Our data from the HFD system demonstrated that MdMs assemble into aggregates/hCLS, and this may be protective against fibrosis. However, as a HFD induces a mild

(G) Ly6C$^{hi}$ monocyte counts in the liver.
(H) Flow plot of F4/80$^{hi}$, CD11b$^{int}$ macrophages where red and green text indicate two phenotypes observed in *Ccr2* KO mice.
(I) Quantification of indicated macrophage populations in WT and KO mice. The red and green symbols indicate the phenotype of the mice from (H).
(J and K) Quantification of C-LAM number as an absolute value (J) and as a percentage of the Tim4$^{neg}$ macrophages (K). Each dot represents an individual mouse, and the bar reflects the mean.
The data represent three independent experiments with n = 3–17 mice/group. The p values are shown. Scale bars, 30 μm.

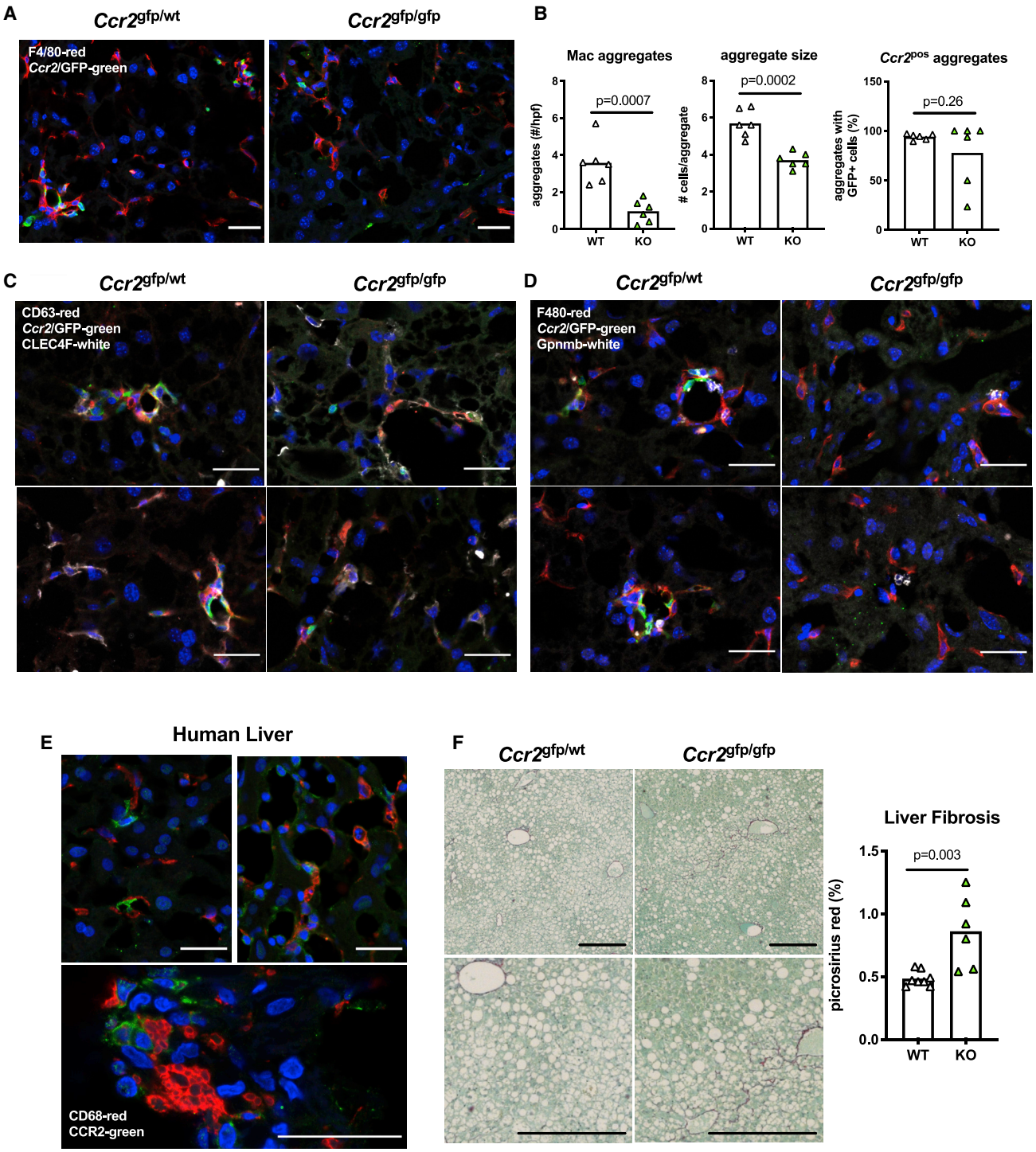


**Figure 6. *Ccr2* Deficiency Leads to Reduced Macrophage Aggregate Formation and Increased Fibrosis**

(A and B) IF images (A) of *Ccr2* WT and KO mice stained for F4/80 and *Ccr2*-GFP and (B) quantification of macrophage aggregates, aggregate size, and number with *Ccr2*-GFP-expressing cells.

(C and D) Images of macrophage aggregates from WT and KO mice stained for expression of CD63 (C) and Gpnmb (D).

(E) Liver tissue from humans with NAFLD stained with antibodies to CD68 (red) and CCR2 (green).

(F) Representative picrosirius red staining (PRS) of liver sections from WT and KO mice at low (top panels) and high power (bottom panels) with quantification of PRS area (right plot). Each dot represents an individual mouse, and the bar reflects the mean.

The data represent two independent experiments with n = 6–8 mice/group. The p values are shown. Scale bars, 30 μm (A and C–E), 250 μm (F).

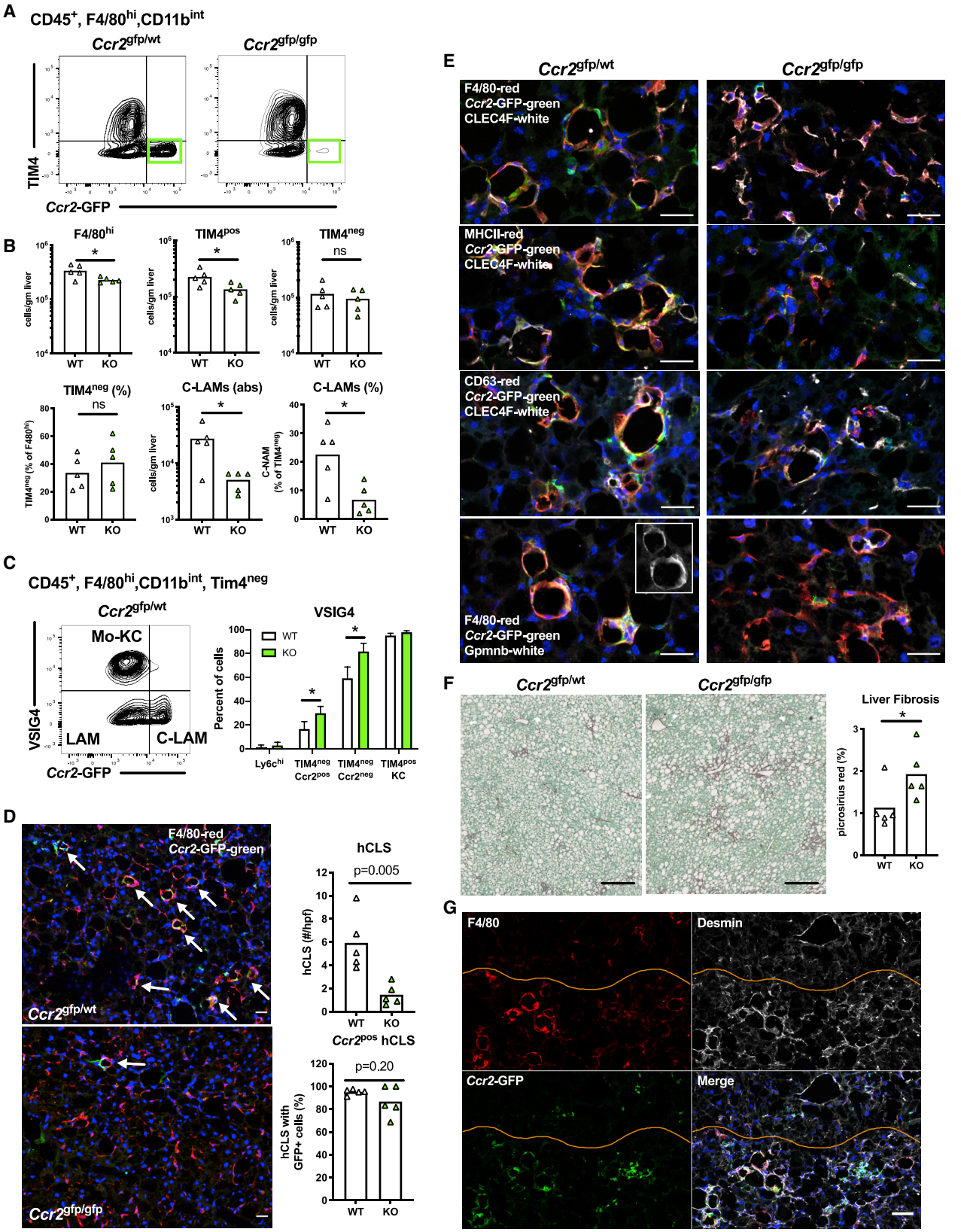


(legend on next page)

inflammatory/fibrotic response, we aimed to strengthen our findings using the fructose, palmitate, cholesterol (FPC) diet, which has been shown to induce more extensive liver inflammation and fibrosis (Wang et al., 2016). After 16 weeks of FPC diet feeding, there was no difference in body weight or liver size between WT and KO mice (Figures S7E–S7G). Similar to what was observed in a subset of mice on a HFD, the number and percentage of total TIM4$^{neg}$ macrophages that accumulated in the livers was similar in both genotypes. However, TIM4$^{pos}$ cells were slightly decreased in the KO animals (Figures 7A and 7B). FPC-fed *Ccr2* KO mice also had a dramatic decrease in the number of Ly6C$^{hi}$ monocytes and C-LAMs compared to WT animals (Figures 7A and 7B).

Although we observed few Mo-KCs in our scRNA-seq using the HFD model, the progressive increase in TIM4$^{neg}$, *Cx3cr1*$^{lo}$ macrophages and decrease in TIM4$^{pos}$ KCs suggested that both LAMs and Mo-KCs could reside in the TIM4$^{neg}$, *Cx3cr1*$^{lo}$ gate. To directly quantify Mo-KCs and to determine whether they were differentially impacted by loss of *Ccr2* in NASH, we assessed expression of CLEC2 and VSIG4 among the TIM4$^{neg}$ macrophages (Scott et al., 2016). CLEC2 has been described as a very early marker of Mo-KCs; however, it remains unclear whether all CLEC2$^{pos}$ cells are destined to become Mo-KCs (Tran et al., 2020). VSIG4 was used a KC marker instead of CLEC4F to identify Mo-KCs as we found that antibodies against this marker were superior for flow cytometry. However, using *Clec4f*-Cre x *Rosa*$^{TdT}$ animals, we confirmed that CLEC4F and VSIG4 largely identify the same cells (Figure S7B). CLEC2 was expressed on ~95% of F4/80$^{hi}$ macrophages and a small subset of Ly6C$^{hi}$ monocytes. Among the TIM4$^{neg}$ macrophages, VSIG4 was expressed on ~65% of *Ccr2*$^{lo}$ macrophages and ~10% of *Ccr2*$^{hi}$ cells (Figure 7C; Figure S7A). Thus, with this diet model ~50% of the TIM4$^{neg}$ macrophages were Mo-KCs. In *Ccr2* KO mice, the majority of TIM4$^{neg}$ cells expressed VSIG4 suggesting that a greater percentage of MdMs were Mo-KCs (Figure 7C). Together these findings demonstrate that (1) TIM4$^{neg}$ macrophages consist of C-LAMs, LAMs, and Mo-KCs that can be distinguished by the expression of *Ccr2* and VSIG4, and (2) *Ccr2* deficiency does not appear to impact the emergence of Mo-KCs in NASH.

To evaluate the consequences of *Ccr2* loss of function on hCLS formation in this model, we performed IF. In WT mice, hCLSs were abundant, whereas the number of these structures was dramatically decreased in the livers of KO mice (Figure 7D). The majority of hCLSs contained C-LAMS in both WT and KO mice, again suggesting an important role for these cells in aggregate formation (Figure 7D). Similar to previous reports (Remmerie et al., 2020), we found that antibodies for the LAM markers Gpnmb and CD63 did not work well via flow cytometry. Therefore, we again employed IF to assess the appearance and distribution of Mo-KCs, C-LAMs, and LAMs in the liver. In WT animals, the majority of macrophages in hCLSs were negative or weakly positive for CLEC4F expression; however, CLEC4F$^{hi}$ cells were occasionally incorporated into these structures (Figure 7E; Figure S7D). In KO mice, macrophage aggregates/hCLSs were rare, and the staining for CLEC4F and F4/80 generally co-localized (Figure 7E). MHCII expression was again higher in macrophages within hCLSs, including some cells with higher levels of CLEC4F expression (Figure 7E). This is consistent with our data that Mo-KCs have higher MHCII expression compared to TIM4$^{pos}$ KCs (Figure S7C). In *Ccr2* KO mice, cells with high expression of MHCII were present but no longer localized to hCLSs (Figure 7E). The expression of the LAM marker CD63 again concentrated in hCLSs and was rarely seen outside these structures or in CLEC4F$^{hi}$ cells in WT mice. However, low-level CLEC4F staining was present in some CD63$^{pos}$ macrophages. In KO mice, CD63-expressing cells were sparse and no longer localized to hCLSs (Figure 7E; Figure S7D). In addition, the CD63 staining pattern in positive cells present in KO mice was cytoplasmic and punctate, consistent with the known lysosomal location of this tetraspanin (Pols and Klumperman, 2009). These observations were confirmed with Gpnmb, which was also enriched in macrophages within hCLSs in WT mice and decreased in *Ccr2* KO mice (Figure 7E). Co-staining of tissue for Gpnmb and CLEC4F revealed that these markers did not co-localize, in line with the notion that hepatic LAMs and Mo-KCs are distinct macrophage subsets (Figure 7E; Figure S7D). In summary, the loss of *Ccr2* decreases C-LAM and LAM number in the tissue and prevents the appropriate assembly of these cells into hCLSs.

To assess the consequences of disrupting MdM development and hCLS formation on tissue fibrosis, we again performed PRS staining to quantify tissue collagen. In line with the fibrogenic nature of FPC diet, the PRS area in WT mice was nearly double that observed with a HFD (Figure 6F versus 7F). Like the HFD-fed mice, the loss of *Ccr2* resulted in increased fibrosis compared to WT animals. Stellate cells are the primary collagen producing cell in the liver (Mederacke et al., 2013). Given recent data suggesting that MdMs may reside in regions of stellate cell expansion (Remmerie et al., 2020) and our findings that tissue fibrosis

**Figure 7. *Ccr2* KO Mice Have Impaired Formation of hCLSs and Increased Fibrosis on a NASH Diet**

(A) Flow-cytometry assessment of macrophages isolated from WT and KO mice fed FPC diet for 16 weeks. Images shown are gated on CD45$^{+}$, F4/80$^{hi}$, CD11b$^{int}$ cells. The green box indicates C-LAMs.

(B) Quantification of the indicated macrophage subsets.

(C) Representative flow plot and quantification of VSIG4 staining for the indicated macrophage populations in WT (white bars) and KO mice (green bars).

(D) Liver sections were stained with antibodies to GFP and F4/80 to identify hCLSs (arrows). Quantification of hCLSs per high-powered field (hpf; top graph) and percentage of hCLSs containing GFP-expressing cells (bottom graph) are shown.

(E) Imaging of hCLSs and macrophage subsets from WT and KO mice stained with antibodies against F4/80, CLEC4F, MHCII, CD63, and Gpnmb as indicated.

(F) Representative images of PRS imaging from WT and KO mice on FPC diet. Quantification of PRS area is shown in the right panel.

(G) IF montage of *Ccr2*-GFP, F4/80, and desmin. The orange line indicates the separation of a desmin-rich area (below) from more typical stellate cell distribution (above).

The data represent two independent experiments with n = 5–6 group. The bars represent with mean and each dot is an individual mouse. *$p < 0.05$. Scale bars, 30 μM (D, E, and G) and 250 μm (F).

was increased with loss of hCLSs, we co-stained for stellate cells and macrophages. We found that C-NAMs/LAMs preferentially formed hCLSs in regions of stellate cell expansion (Figure 7G). Thus, our findings confirm that hepatic C-LAMs/LAMs appear in regions of the liver with increased numbers of stellate cells and assemble into hCLSs, events that appear to modulate liver fibrosis during NASH.

## DISCUSSION

NAFLD is a common complication of obesity; however, the events that drive progression from simple steatosis to more severe inflammatory/fibrotic disease are not well understand. In this study, we evaluated intrahepatic macrophage composition in a mouse model of obesity with NAFLD and in a model of NASH. The objectives of this study were to (1) characterize the changes in recruited versus resident macrophages during NAFLD and NASH, (2) define the heterogeneity and phenotypes of these macrophage populations, and (3) assess the function of these macrophage subsets in liver pathology.

Over the past decade, it has become increasingly apparent that there are considerable differences in the origin, proliferative capacity, and biologic function between resident and recruited macrophages. In addition, tissue niche fosters the development of unique macrophage programming. Understanding macrophage heterogeneity in NAFLD and NASH is of particular interest for its therapeutic potential. Resident KCs are generally identified by their F4/80$^{hi}$, CD11b$^{int}$ phenotype, whereas monocytes/MdMs are CD11b$^{hi}$, F4/80$^{int}$. However, using markers that are more specific for KCs, including TIM4, CLEC4F, and VSIG4, we demonstrate that the composition of "resident" F4/80$^{hi}$ cells evolves significantly during NAFLD progression. Specifically, the number of TIM4$^{pos}$ KCs decreases while the number and percentage of TIM4$^{neg}$ cells in this population increases. Using lineage tracing and fate-mapping approaches, we verified that TIM4$^{neg}$ macrophages were indeed of monocyte origin and not a sub-population of KCs that downregulate this receptor. These findings are consistent with results from a recent study using the methionine-choline deficient model of NASH, which found that fatty liver was associated with a decrease in resident KCs and an increase in TIM4$^{neg}$ macrophages (Devisscher et al., 2017).

In response to resident macrophage depletion, monocytes can enter the liver and take on a KC phenotype (Bonnardel et al., 2019; Sakai et al., 2019; Scott et al., 2016; van de Laar et al., 2016). In addition, monocytes can be recruited in response to tissue damage. In NASH, it is likely that both of these factors drive the recruitment and promote functional heterogeneity of MdMs. To understand the diversity of MdMs, we utilized single-cell and bulk RNA sequencing in conjunction with GFP reporter mice, flow cytometry, and IF. Together these assays confirmed the presence of three major populations of TIM4$^{neg}$, F4/80$^{hi}$ MdMs that accumulate with a HFD. One subset expressed high levels of *Cx3cr1*/*Ccr2* and *Trem2*, another subset had lower expression of *Cx3cr1*/*Ccr2* and progressively higher expression of *Trem2*, *Gpmnb*, *Spp1*, *Cd63*, and *Cd9*, and the third subset had higher expression of CLEC4F/VSIG4. The expression of *GATA6* was not observed in any of these subsets arguing against a peritoneal/serosal origin of these macrophages (Wang and Kubes, 2016). How do these macrophages subsets align with other macrophage populations described in NASH/obesity? Recently, a scRNA-seq analysis of hepatic non-parenchymal cells in NASH described the presence of *Trem2*$^{pos}$ and *Trem2*$^{neg}$ KCs during NASH (Xiong et al., 2019). The *Trem2*$^{pos}$ KCs also expressed *Gpmnb* and *Cd9* and were referred to as NAMs. Although NAMs were initially thought to represent KCs reprogrammed by the high-fat environment, our data confirm that these macrophages are in fact MdMs. In addition, a subset of macrophages isolated from obese adipose tissue, referred to as LAMs, also shares a similar gene-expression profile (Jaitin et al., 2019). The authors of this study also proposed the existence of hepatic LAMs with obesity, which was confirmed in a more recent publication that defined these cells based on their expression of *Spp1*, *Trem2*, *Cd9*, *Cd63*, and *Gpnmb* (Remmerie et al., 2020). To maintain consistency within the field, we opted to refer to the three subsets of MdMs we describe as hepatic C-LAMs, LAMs, and Mo-KCs.

The expression of *Cx3cr1* and *Ccr2* on C-LAMs suggests that they represent monocyte-derived cells that have more recently entered the liver. In line with this idea, C-LAMs also had slightly lower expression of F4/80 and higher surface levels of MHCII and CD11c, a phenotype recently described for monocytes progressing toward macrophage (Bonnardel et al., 2019). Of interest, C-LAMs also express the early KC marker CLEC2 but rarely express VSIG4 or CLEC4F, markers of progressive KC differentiation. The TIM4$^{neg}$, *Cx3cr1*$^{lo}$ macrophages included hepatic LAMs and Mo-KCs, which could be distinguished via flow cytometry based on the expression of VSIG4. However, tissue imaging was required to positively identify LAMs in the liver as antibodies to CD9, CD63, and Gpnmb had limited utility via flow cytometry. *Cx3cr1*/*Ccr2*-GFP reporter mice were also leveraged to aid in the identification of macrophage subsets. Although rare with STD, following HFD exposure *Cx3cr1*/*Ccr2*-expressing cells were abundant in the sinusoids and frequently localized to macrophage aggregates and hCLSs. Macrophages expressing high levels of MHCII, CD63, and Gpmnb also localized to hCLSs. In contrast, the KC marker CLEC4F was usually expressed at low levels on cells in the aggregates. Instead, the CLEC4F$^{hi}$ cells tended to remain in sinusoids as single cells or as a single CLEC4F$^{hi}$ cell within an aggregate. The CLEC4F$^{hi}$ cells rarely co-expressed markers of LAMs arguing that these markers truly define distinct macrophage subsets. C-LAMs/LAMs preferentially formed hCLSs around lipid droplets in regions of stellate cell expansion, and this observation is similar to recent findings that hepatic LAMs tend to localize in stellate cell-rich zones in the liver (Remmerie et al., 2020).

The presence of hCLSs is associated with the transition from simple steatosis to NASH in both mice and humans (Itoh et al., 2013). We utilized *Ccr2* KO mice as a tool to gain insight into the function of MdMs in NASH. Baseline KC number was not impacted by loss of *Ccr2*, yet MdM composition was altered after HFD/FPC diet feeding. In the majority of KO mice TIM4$^{neg}$ macrophage accumulation was similar; however, the C-LAM and LAM populations were reduced. The bulk of TIM4$^{neg}$ cells in KO mice were VSIG4$^{pos}$ Mo-KCs. These findings are consistent with previous data that Mo-KCs can repopulate the resident niche independent of *Ccr2* following KC depletion (Bonnardel

et al., 2019). Together these data suggest that KC loss is one trigger that promotes monocyte recruitment and Mo-KC differentiation during NASH; however, tissue damage and lipid accumulation may promote the recruitment and differentiation of monocytes into C-LAMs and LAMs.

The reduction of C-LAM/LAMs in the *Ccr2* KO model allowed us to gain insight into the the role of these cells in the assembly of hCLSs and whether these structures were beneficial or detrimental to tissue remodeling during NASH. The number and size of macrophage aggregates and hCLSs were dramatically reduced in *Ccr2* KO mice. In addition, *Ccr2*-expressing cells were present in virtually all macrophage aggregates, even in the KO mice. Macrophages expressing LAM markers (high MHCII, CD63, and Gpnmb) co-localized to hCLSs in WT mice but were reduced in number and not a part of aggregates in KO animals. Thus, monocytes recruited to areas of inflammation may preferentially differentiate into C-LAMs/LAMs and assemble into hCLSs. How C-LAMs regulate this process is not well understood. Although we cannot exclude a role for monocyte-derived DCs in the *Ccr2* KO system, the fact that macrophages are enriched in hCLSs coupled with the relatively small change in the cDC2 numbers with *Ccr2* KO argue against these cells as major contributors. The *Ccr2* KO system has its limitations in that it does not allow for mechanistic studies of the specific roles played by distinct monocyte-derived cells in hCLS formation, which will require additional genetic models.

NASH ultimately culminates in liver fibrosis, which can progress to cirrhosis. *Ccr2* KO mice had similar degrees of weight gain, liver steatosis, and tissue damage but decreased accumulation of C-LAMs/LAMs and hCLSs. Therefore, we assessed the impact of this shift in macrophage composition on tissue remodeling. Liver fibrosis was increased in *Ccr2* KO mice in response to a HFD or FPC diet, and the fibrosis was predominantly localized to areas of macrovesicular steatosis, where hCLSs tend to form. These results are intriguing as CCR2$^{pos}$ macrophages are thought to be pro-fibrotic, and CCR2 inhibition has been proposed as a target of therapy for NASH fibrosis. However, the situation is made more complex by the fact that MdMs have been associated with both profibrotic and antifibrotic pathways following acute liver injury (Tacke and Zimmermann, 2014). In fact, loss of *Ccr2* has also been associated with increased fibrosis following toxin-induced acute liver injury (Mitchell et al., 2009). As pharmacologic CCR2 inhibition has been shown to reduce tissue fibrosis, it is also possible that the timing of CCR2 blockade could further influence macrophage composition and alter tissue remodeling (Lefere et al., 2020). Data from obese adipose tissue have shown that disruption of LAMs/CLS worsens metabolic disease. Similarly, in a model of Alzheimer disease TREM2$^{pos}$ macrophage aggregates in the brain help contain amyloid plaques (Jaitin et al., 2019; Ulland et al., 2017). Thus, hCLSs may serve to contain and/or digest damaged areas of liver, which could ultimately reduce fibrosis. *Ccr2* deficiency may also reduce the number macrophages with antifibrotic potential. Our findings are distinct from a previous study suggesting that hCLSs are primarily formed by resident KCs (Itoh et al., 2017). In this study, the authors also used an elegant CD169-DTR system to deplete resident macrophages and demonstrated that hCLS formation was disrupted. However, C-LAMs also express *Siglec1*/CD169, and therefore this subset of macrophages would also be depleted. In addition, they report CD11c expression on "resident" macrophages found in hCLSs. However, in our study, CD11c was most robustly expressed by C-LAMs and was absent from resident KCs.

While this manuscript was under revision, three other papers were published investigating macrophage heterogeneity during NASH (Remmerie et al., 2020; Seidman et al., 2020; Tran et al., 2020). Our findings are largely consistent with these studies and, together, they all demonstrate that resident KCs are lost during NASH progression and MdMs cells enter the liver, where they respond to niche-specific and inflammatory cues to become Mo-KCs or hepatic C-LAMs/LAMs. In Tran et al. (2020), all CLEC2$^{pos}$ cells were referred to as Mo-KCs; however, they also observed a significant number of CLEC2$^{pos}$, VSIG4$^{neg}$ macrophages in the liver during NASH. Moreover, RNA-seq of "Mo-KCs" in their study revealed enhanced expression of genes found in C-LAMS/LAMs, including *Cx3cr1*, *Itgax*, *Gpnmb*, *Cd9*, *Trem2*, and MHC class II genes, suggesting that C-LAMs and LAMs also may have been present among these cells. Our data are also similar to the data in the study by Remmerie et al. (2020) in that we found C-LAMs/LAMs express Osteopontin (*Spp1*) and preferentially localize to regions of stellate cell expansion where they form into hCLSs. Based on imaging and RNA-seq, C-LAMs/LAMs and Mo-KCs appear to occupy the sinusoidal niche and express early liver niche genes (*Nr1h3*/LXR, *Id3*, *Fabp7*, and *Clec1b*/CLEC2). It is currently unclear what signals specify macrophages to become a Mo-KC versus a C-LAM/LAM, but it is attractive to speculate that stellate cells may contribute to macrophage-fate decisions.

Understanding the transition of NAFLD to NASH has important physiological and clinical implications. Macrophages contribute to tissue remodeling and the response to injury, which are key factors in the progression of fatty liver disease (Kazankov et al., 2019). The results from the present study enhance our understanding of macrophage diversity in NASH. In contrast to current dogma, our data demonstrate that resident KCs are lost during the progression of steatosis to NASH and MdMs begin to populate the liver. Within these recruited subsets, C-LAMs and LAMs contribute to hCLS formation and modulate liver fibrosis.

## STAR★METHODS

Detailed methods are provided in the online version of this paper and include the following:

- KEY RESOURCES TABLE
- RESOURCE AVAILABILITY
  - Lead Contact
  - Materials Availability
  - Data and Code Availability
- EXPERIMENTAL MODEL AND SUBJECT DETAILS
  - *In vivo* animal studies
  - Human samples
- METHOD DETAILS
  - GTT and ITT

- Single cell preparation of adipose and liver tissue for flow cytometry
- Total RNA and qRT-PCR
- Histology and Immunofluorescence
- Transmission electron microscopy (TEM)
- RNA sequencing

- QUANTIFICATION AND STATISTICAL ANALYSIS

## SUPPLEMENTAL INFORMATION

Supplemental Information can be found online at https://doi.org/10.1016/j.celrep.2020.108626.

## ACKNOWLEDGMENTS

This work was supported by NIH grants RO1 DK11003401 (J.D.S.), ADA 118-IBS280 (J.D.S.), and R01 DK104735 (B.N.F.) and support from the Pershing Square Foundation (S.K.). The core services of the Diabetes Research Center (P30 DK020579) and the Nutrition and Obesity Research Center (P30 DK56341) at Washington University School of Medicine also supported this work.

## AUTHOR CONTRIBUTIONS

Conceptualization, S.D., G.K., and J.D.S.; Methodology S.D., G.K., A.G., M.A., and J.D.S.; Investigation, S.D., A.G., G.K., L.H., M.C., J.B., K.H.L., and J.D.S.; Writing – Original Draft, J.D.S.; Writing – Review & Editing, S.D., A.G., J.W.B., S.K., B.N.F., M.A., and J.D.S.; Revision Experiments, Review, and Editing, S.D., A.G., A.E.F., and J.D.S.

## DECLARATION OF INTERESTS

A.E.F. is co-inventor on pending and issued patents filed by the Cleveland Clinic and UCSD that refer to the use of biomarkers and therapies in inflammatory and fibrotic disorders. Scientific Founder: Jecure Therapeutics, Elgia Therapeutics. Consultant/Advisory Board: Gilead, GSK, Merck, Ferring Pharmaceutical, Centurion BioPharma, Oppilan Pharma. The remaining authors have no interests to declare.

Received: January 15, 2020
Revised: October 22, 2020
Accepted: December 18, 2020
Published: January 12, 2021

## REFERENCES

Bajpai, G., Bredemeyer, A., Li, W., Zaitsev, K., Koenig, A.L., Lokshina, I., Mohan, J., Ivey, B., Hsiao, H.M., Weinheimer, C., et al. (2019). Tissue Resident CCR2- and CCR2+ Cardiac Macrophages Differentially Orchestrate Monocyte Recruitment and Fate Specification Following Myocardial Injury. Circ. Res. *124*, 263–278.

Beattie, L., Sawtell, A., Mann, J., Frame, T.C.M., Teal, B., de Labastida Rivera, F., Brown, N., Walwyn-Brown, K., Moore, J.W.J., MacDonald, S., et al. (2016). Bone marrow-derived and resident liver macrophages display unique transcriptomic signatures but similar biological functions. J. Hepatol. *65*, 758–768.

Bonnardel, J., T'Jonck, W., Gaublomme, D., Browaeys, R., Scott, C.L., Martens, L., Vanneste, B., De Prijck, S., Nedospasov, S.A., Kremer, A., et al. (2019). Stellate Cells, Hepatocytes, and Endothelial Cells Imprint the Kupffer Cell Identity on Monocytes Colonizing the Liver Macrophage Niche. Immunity *51*, 638–654.

Brunt, E.M., Janney, C.G., Di Bisceglie, A.M., Neuschwander-Tetri, B.A., and Bacon, B.R. (1999). Nonalcoholic steatohepatitis: a proposal for grading and staging the histological lesions. Am. J. Gastroenterol. *94*, 2467–2474.

Devisscher, L., Scott, C.L., Lefere, S., Raevens, S., Bogaerts, E., Paridaens, A., Verhelst, X., Geerts, A., Guilliams, M., and Van Vlierberghe, H. (2017). Non-alcoholic steatohepatitis induces transient changes within the liver macrophage pool. Cell. Immunol. *322*, 74–83.

Dobin, A., Davis, C.A., Schlesinger, F., Drenkow, J., Zaleski, C., Jha, S., Batut, P., Chaisson, M., and Gingeras, T.R. (2013). STAR: ultrafast universal RNA-seq aligner. Bioinformatics *29*, 15–21.

Epelman, S., Lavine, K.J., Beaudin, A.E., Sojka, D.K., Carrero, J.A., Calderon, B., Brija, T., Gautier, E.L., Ivanov, S., Satpathy, A.T., et al. (2014). Embryonic and adult-derived resident cardiac macrophages are maintained through distinct mechanisms at steady state and during inflammation. Immunity *40*, 91–104.

Fabbrini, E., Sullivan, S., and Klein, S. (2010). Obesity and nonalcoholic fatty liver disease: biochemical, metabolic, and clinical implications. Hepatology *51*, 679–689.

Gomez Perdiguero, E., Klapproth, K., Schulz, C., Busch, K., Azzoni, E., Crozet, L., Garner, H., Trouillet, C., de Bruijn, M.F., Geissmann, F., and Rodewald, H.R. (2015). Tissue-resident macrophages originate from yolk-sac-derived erythro-myeloid progenitors. Nature *518*, 547–551.

Guillot, A., and Tacke, F. (2019). Liver Macrophages: Old Dogmas and New Insights. Hepatol. Commun. *3*, 730–743.

Hill, D.A., Lim, H.W., Kim, Y.H., Ho, W.Y., Foong, Y.H., Nelson, V.L., Nguyen, H.C.B., Chegireddy, K., Kim, J., Habertheuer, A., et al. (2018). Distinct macrophage populations direct inflammatory versus physiological changes in adipose tissue. Proc. Natl. Acad. Sci. USA *115*, E5096–E5105.

Huang, W., Metlakunta, A., Dedousis, N., Zhang, P., Sipula, I., Dube, J.J., Scott, D.K., and O'Doherty, R.M. (2010). Depletion of liver Kupffer cells prevents the development of diet-induced hepatic steatosis and insulin resistance. Diabetes *59*, 347–357.

Ioannou, G.N., Haigh, W.G., Thorning, D., and Savard, C. (2013). Hepatic cholesterol crystals and crown-like structures distinguish NASH from simple steatosis. J. Lipid Res. *54*, 1326–1334.

Ioannou, G.N., Van Rooyen, D.M., Savard, C., Haigh, W.G., Yeh, M.M., Teoh, N.C., and Farrell, G.C. (2015). Cholesterol-lowering drugs cause dissolution of cholesterol crystals and disperse Kupffer cell crown-like structures during resolution of NASH. J. Lipid Res. *56*, 277–285.

Ioannou, G.N., Subramanian, S., Chait, A., Haigh, W.G., Yeh, M.M., Farrell, G.C., Lee, S.P., and Savard, C. (2017). Cholesterol crystallization within hepatocyte lipid droplets and its role in murine NASH. J. Lipid Res. *58*, 1067–1079.

Itoh, M., Kato, H., Suganami, T., Konuma, K., Marumoto, Y., Terai, S., Sakugawa, H., Kanai, S., Hamaguchi, M., Fukaishi, T., et al. (2013). Hepatic crown-like structure: a unique histological feature in non-alcoholic steatohepatitis in mice and humans. PLoS ONE *8*, e82163.

Itoh, M., Suganami, T., Kato, H., Kanai, S., Shirakawa, I., Sakai, T., Goto, T., Asakawa, M., Hidaka, I., Sakugawa, H., et al. (2017). CD11c+ resident macrophages drive hepatocyte death-triggered liver fibrosis in a murine model of nonalcoholic steatohepatitis. JCI Insight *2*, e92902.

Jaitin, D.A., Adlung, L., Thaiss, C.A., Weiner, A., Li, B., Descamps, H., Lundgren, P., Bleriot, C., Liu, Z., Deczkowska, A., et al. (2019). Lipid-Associated Macrophages Control Metabolic Homeostasis in a Trem2-Dependent Manner. Cell *178*, 686–698.

Kazankov, K., Jørgensen, S.M.D., Thomsen, K.L., Møller, H.J., Vilstrup, H., George, J., Schuppan, D., and Grønbæk, H. (2019). The role of macrophages in nonalcoholic fatty liver disease and nonalcoholic steatohepatitis. Nat. Rev. Gastroenterol. Hepatol. *16*, 145–159.

Kleiner, D.E., Brunt, E.M., Van Natta, M., Behling, C., Contos, M.J., Cummings, O.W., Ferrell, L.D., Liu, Y.C., Torbenson, M.S., Unalp-Arida, A., et al.; Nonalcoholic Steatohepatitis Clinical Research Network (2005). Design and validation of a histological scoring system for nonalcoholic fatty liver disease. Hepatology *41*, 1313–1321.

Krenkel, O., Hundertmark, J., Abdallah, A.T., Kohlhepp, M., Puengel, T., Roth, T., Branco, D.P.P., Mossanen, J.C., Luedde, T., Trautwein, C., et al. (2020). Myeloid cells in liver and bone marrow acquire a functionally distinct inflammatory phenotype during obesity-related steatohepatitis. Gut *69*, 551–563.

Lavine, K.J., Epelman, S., Uchida, K., Weber, K.J., Nichols, C.G., Schilling, J.D., Ornitz, D.M., Randolph, G.J., and Mann, D.L. (2014). Distinct macrophage lineages contribute to disparate patterns of cardiac recovery and remodeling in the neonatal and adult heart. Proc. Natl. Acad. Sci. USA *111*, 16029–16034.

Lefere, S., Devisscher, L., and Tacke, F. (2020). Targeting CCR2/5 in the treatment of nonalcoholic steatohepatitis (NASH) and fibrosis: opportunities and challenges. Expert Opin. Investig. Drugs *29*, 89–92.

Liao, Y., Smyth, G.K., and Shi, W. (2014). featureCounts: an efficient general purpose program for assigning sequence reads to genomic features. Bioinformatics *30*, 923–930.

Liu, R., Holik, A.Z., Su, S., Jansz, N., Chen, K., Leong, H.S., Blewitt, M.E., Asselin-Labat, M.L., Smyth, G.K., and Ritchie, M.E. (2015). Why weight? Modelling sample and observational level variability improves power in RNA-seq analyses. Nucleic Acids Res. *43*, e97.

McCarthy, D.J., Chen, Y., and Smyth, G.K. (2012). Differential expression analysis of multifactor RNA-Seq experiments with respect to biological variation. Nucleic Acids Res. *40*, 4288–4297.

McGettigan, B., McMahan, R., Orlicky, D., Burchill, M., Danhorn, T., Francis, P., Cheng, L.L., Golden-Mason, L., Jakubzick, C.V., and Rosen, H.R. (2019). Dietary Lipids Differentially Shape Nonalcoholic Steatohepatitis Progression and the Transcriptome of Kupffer Cells and Infiltrating Macrophages. Hepatology *70*, 67–83.

Mederacke, I., Hsu, C.C., Troeger, J.S., Huebener, P., Mu, X., Dapito, D.H., Pradere, J.P., and Schwabe, R.F. (2013). Fate tracing reveals hepatic stellate cells as dominant contributors to liver fibrosis independent of its aetiology. Nat. Commun. *4*, 2823.

Mitchell, C., Couton, D., Couty, J.P., Anson, M., Crain, A.M., Bizet, V., Rénia, L., Pol, S., Mallet, V., and Gilgenkrantz, H. (2009). Dual role of CCR2 in the constitution and the resolution of liver fibrosis in mice. Am. J. Pathol. *174*, 1766–1775.

Neyrinck, A.M., Cani, P.D., Dewulf, E.M., De Backer, F., Bindels, L.B., and Delzenne, N.M. (2009). Critical role of Kupffer cells in the management of diet-induced diabetes and obesity. Biochem. Biophys. Res. Commun. *385*, 351–356.

Pols, M.S., and Klumperman, J. (2009). Trafficking and function of the tetraspanin CD63. Exp. Cell Res. *315*, 1584–1592.

Reid, D.T., Reyes, J.L., McDonald, B.A., Vo, T., Reimer, R.A., and Eksteen, B. (2016). Kupffer Cells Undergo Fundamental Changes during the Development of Experimental NASH and Are Critical in Initiating Liver Damage and Inflammation. PLoS ONE *11*, e0159524.

Remmerie, A., Martens, L., Thoné, T., Castoldi, A., Seurinck, R., Pavie, B., Roels, J., Vanneste, B., De Prijck, S., Vanhockerhout, M., et al. (2020). Osteopontin Expression Identifies a Subset of Recruited Macrophages Distinct from Kupffer Cells in the Fatty Liver. Immunity *53*, 641–657.

Ritchie, M.E., Phipson, B., Wu, D., Hu, Y., Law, C.W., Shi, W., and Smyth, G.K. (2015). limma powers differential expression analyses for RNA-sequencing and microarray studies. Nucleic Acids Res. *43*, e47.

Robinson, M.D., McCarthy, D.J., and Smyth, G.K. (2010). edgeR: a Bioconductor package for differential expression analysis of digital gene expression data. Bioinformatics *26*, 139–140.

Rogoff, T.M., and Lipsky, P.E. (1981). Role of the Kupffer cells in local and systemic immune responses. Gastroenterology *80*, 854–860.

Sakai, M., Troutman, T.D., Seidman, J.S., Ouyang, Z., Spann, N.J., Abe, Y., Ego, K.M., Bruni, C.M., Deng, Z., Schlachetzki, J.C.M., et al. (2019). Liver-Derived Signals Sequentially Reprogram Myeloid Enhancers to Initiate and Maintain Kupffer Cell Identity. Immunity *51*, 655–670.

Schulz, C., Gomez Perdiguero, E., Chorro, L., Szabo-Rogers, H., Cagnard, N., Kierdorf, K., Prinz, M., Wu, B., Jacobsen, S.E., Pollard, J.W., et al. (2012). A lineage of myeloid cells independent of Myb and hematopoietic stem cells. Science *336*, 86–90.

Scott, C.L., Zheng, F., De Baetselier, P., Martens, L., Saeys, Y., De Prijck, S., Lippens, S., Abels, C., Schoonooghe, S., Raes, G., et al. (2016). Bone marrow-derived monocytes give rise to self-renewing and fully differentiated Kupffer cells. Nat. Commun. *7*, 10321.

Seidman, J.S., Troutman, T.D., Sakai, M., Gola, A., Spann, N.J., Bennett, H., Bruni, C.M., Ouyang, Z., Li, R.Z., Sun, X., et al. (2020). Niche-Specific Reprogramming of Epigenetic Landscapes Drives Myeloid Cell Diversity in Nonalcoholic Steatohepatitis. Immunity *52*, 1057–1074.

Sierro, F., Evrard, M., Rizzetto, S., Melino, M., Mitchell, A.J., Florido, M., Beattie, L., Walters, S.B., Tay, S.S., Lu, B., et al. (2017). A Liver Capsular Network of Monocyte-Derived Macrophages Restricts Hepatic Dissemination of Intraperitoneal Bacteria by Neutrophil Recruitment. Immunity *47*, 374–388.

Stienstra, R., Saudale, F., Duval, C., Keshtkar, S., Groener, J.E., van Rooijen, N., Staels, B., Kersten, S., and Müller, M. (2010). Kupffer cells promote hepatic steatosis via interleukin-1beta-dependent suppression of peroxisome proliferator-activated receptor alpha activity. Hepatology *51*, 511–522.

Tacke, F., and Zimmermann, H.W. (2014). Macrophage heterogeneity in liver injury and fibrosis. J. Hepatol. *60*, 1090–1096.

Tandra, S., Yeh, M.M., Brunt, E.M., Vuppalanchi, R., Cummings, O.W., Ünalp-Arida, A., Wilson, L.A., and Chalasani, N. (2011). Presence and significance of microvesicular steatosis in nonalcoholic fatty liver disease. J. Hepatol. *55*, 654–659.

Tosello-Trampont, A.C., Landes, S.G., Nguyen, V., Novobrantseva, T.I., and Hahn, Y.S. (2012). Kuppfer cells trigger nonalcoholic steatohepatitis development in diet-induced mouse model through tumor necrosis factor-α production. J. Biol. Chem. *287*, 40161–40172.

Tran, S., Baba, I., Poupel, L., Dussaud, S., Moreau, M., Gélineau, A., Marcelin, G., Magréau-Davy, E., Ouhachi, M., Lesnik, P., et al. (2020). Impaired Kupffer Cell Self-Renewal Alters the Liver Response to Lipid Overload during Non-alcoholic Steatohepatitis. Immunity *53*, 627–640.

Ulland, T.K., Song, W.M., Huang, S.C., Ulrich, J.D., Sergushichev, A., Beatty, W.L., Loboda, A.A., Zhou, Y., Cairns, N.J., Kambal, A., et al. (2017). TREM2 Maintains Microglial Metabolic Fitness in Alzheimer's Disease. Cell *170*, 649–663.

van de Laar, L., Saelens, W., De Prijck, S., Martens, L., Scott, C.L., Van Isterdael, G., Hoffmann, E., Beyaert, R., Saeys, Y., Lambrecht, B.N., and Guilliams, M. (2016). Yolk Sac Macrophages, Fetal Liver, and Adult Monocytes Can Colonize an Empty Niche and Develop into Functional Tissue-Resident Macrophages. Immunity *44*, 755–768.

Vernon, G., Baranova, A., and Younossi, Z.M. (2011). Systematic review: the epidemiology and natural history of non-alcoholic fatty liver disease and non-alcoholic steatohepatitis in adults. Aliment. Pharmacol. Ther. *34*, 274–285.

Wang, J., and Kubes, P. (2016). A Reservoir of Mature Cavity Macrophages that Can Rapidly Invade Visceral Organs to Affect Tissue Repair. Cell *165*, 668–678.

Wang, L., Wang, S., and Li, W. (2012). RSeQC: quality control of RNA-seq experiments. Bioinformatics *28*, 2184–2185.

Wang, X., Zheng, Z., Caviglia, J.M., Corey, K.E., Herfel, T.M., Cai, B., Masia, R., Chung, R.T., Lefkowitch, J.H., Schwabe, R.F., and Tabas, I. (2016). Hepatocyte TAZ/WWTR1 Promotes Inflammation and Fibrosis in Nonalcoholic Steatohepatitis. Cell Metab. *24*, 848–862.

Wree, A., Broderick, L., Canbay, A., Hoffman, H.M., and Feldstein, A.E. (2013). From NAFLD to NASH to cirrhosis-new insights into disease mechanisms. Nat. Rev. Gastroenterol. Hepatol. *10*, 627–636.

Xiong, X., Kuang, H., Ansari, S., Liu, T., Gong, J., Wang, S., Zhao, X.Y., Ji, Y., Li, C., Guo, L., et al. (2019). Landscape of Intercellular Crosstalk in Healthy and NASH Liver Revealed by Single-Cell Secretome Gene Analysis. Mol. Cell *75*, 644–660.

Yona, S., Kim, K.W., Wolf, Y., Mildner, A., Varol, D., Breker, M., Strauss-Ayali, D., Viukov, S., Guilliams, M., Misharin, A., et al. (2013). Fate mapping reveals origins and dynamics of monocytes and tissue macrophages under homeostasis. Immunity *38*, 79–91.

## STAR★METHODS

### KEY RESOURCES TABLE

| REAGENT or RESOURCE | SOURCE | IDENTIFIER |
|---|---|---|
| Antibodies | | |
| Rat monoclonal CD11b-APC-Cy7 (clone M1/70) | Biolegend | Cat# 101226; RRID:AB_830642 |
| Armenian Hamster monoclonal CD11c-BV711 (clone N418) | Biolegend | Cat# 117349; RRID:AB_6253905 |
| Rat monoclonal CD45-PerCP-Cy5.5 (clone 30-F11) | Biolegend | Cat# 103132; RRID:AB_348930 |
| Rat monoclonal CD45-BUV395 (clone 30-F11) | BD Biosciences | Cat# 564279; RRID:AB_2651134 |
| Rat monoclonal F4/80-AF647 (clone BM8) | Biolegend | Cat# 123122; RRID:AB_893480 |
| Rat monoclonal Ly6C-PE-Cy7 (clone HK1.4) | Biolegend | Cat# 128018; RRID:AB_1732082 |
| Rat monoclonal Ly6C-Pacific blue (clone HK1.4) | Biolegend | Cat# 128014; RRIS:AB_1732079 |
| Rat monoclonal MHCII-BV605 (clone M5/114.15.2) | Biolegend | Cat# 107639; RRID:AB_2565894 |
| Rat monoclonal MHCII-PE (clone M5/114.15.2) | Biolegend | Cat# 107608; RRID:AB_313323 |
| Rat monoclonal TIM4-BV421 (clone 21H12) | BD Biosciences | Cat# 742773; RRID:AB_2741037 |
| Rat monoclonal TIM4-PE-Cy7 (clone RMT4-54) | Biolegend | Cat# 130010; RRID:AB_2565719 |
| Mouse monoclonal CD64-BV605 (clone X54-5/7.1) | Biolegend | Cat# 139323; RRID:AB_2629778 |
| Rat monoclonal VSIG4-PeCy7 (clone NLA14) | Invitrogen-ThermoFisher | Cat# 25-5752-82; RRID:AB_2637431 |
| Rat monoclonal VSIG4-PE (clone NLA14) | Invitrogen-ThermoFisher | Cat# 12-5752-82; RRID:AB_2784625 |
| Rat monoclonal CLEC2-PE (clone 17D9) | Biolegend | Cat# 146104;RRID:AB_2562383 |
| Chicken polyclonal GFP - unconjugated | Abcam | Cat# ab13970; RRID:AB_300798 |
| Rat monoclonal F4/80 - unconjugated (clone BM8) | Invitrogen-ThermoFisher | Cat# 13-4801-85; RRID:AB_466658 |
| Rat monoclonal TIM4 - unconjugated (clone RMT4-54) | Biolegend | Cat# 130002; RRID:AB_1227802 |
| Goat polyclonal CLEC4F - unconjugated | RD Systems | Cat# AF2784; RRID:AB_2081339 |
| Rat monoclonal MHCII - unconjugated (clone M5/114.15.2) | Biolegend | Cat# 107601; RRID:AB_313316 |
| Rat monoclonal CD63 - unconjugated (clone NGV-4) | Biolegend | Cat# 143902; RRID:AB_11204263 |
| Rabbit monoclonal Gpnmb - unconjugated (clone EPR18226-147) | Abcam | Cat# 188222 |
| Mouse monoclonal CCR2 - unconjugated (clone 7A7) | Abcam | Cat# ab176390 |
| Rabbit monoclonal CD68 – unconjugated (clone EPR20545) | Abcam | Cat# ab213363; RRID:AB_2801637 |
| Goat anti-chicken AF488 | Abcam | Cat# ab150173; RRID:AB_2827653 |
| Donkey anti-chicken AF488 | Jackson Immunoresearch | Cat# 703-545-155; RRID:AB_0234375 |
| Donkey anti-rat AF594 | Invitrogen-ThermoFisher | Cat# A21209; RRID:AB_2535795 |
| Donkey anti-rat AF488 | Invitrogen-ThermoFisher | Cat# A21208; RRID:AB_2535794 |
| Donkey anti-rabbit AF647 | Jackson Immunoresearch | Cat# 711-605-152; RRID:AB_2492288 |

(*Continued on next page*)

*Continued*

| REAGENT or RESOURCE | SOURCE | IDENTIFIER |
|---|---|---|
| Donkey anti-goat AF647 | Jackson Immunoresearch | Cat# 705-605-003; RRID:AB_2340436 |
| Goat anti-mouse AF488 | Jackson Immunoresearch | Cat# 115-545-003; RRID:AB_2338840 |
| Goat anti-rabbit AF594 | Jackson Immunoresearch | Cat# 111-585-003; RRID:AB_2338059 |
| **Biological Samples** | | |
| Human liver tissue | Washington University in St. Louis | NCT003701828 |
| **Chemicals, Peptides, and Recombinant Proteins** | | |
| Collagenase A | Sigma | Cat# C5138 |
| DNase I | Sigma | Cat# 10104159001 |
| Percoll | Sigma | Cat# GE17-0891-02 |
| Zombie Aqua | Biolegend | Cat# 423101 |
| Fc Block | BD Biosciences | Cat# 553143 |
| D-(+)-Glucose | Sigma | Cat# G8270 |
| Insulin | Humulin | Cat# HI-210 |
| DMEM | Sigma | Cat# D5671 |
| L-glutamine | Sigma | Cat# G7513 |
| P/S | GIBCO | Cat# 15140-122 |
| FBS | Sigma | Cat# F2442 |
| MDH | Abcepta | Cat# SM1000a |
| 10% Neutral buffered formalin | Sigma | Cat# HT5011-1CS |
| Tissue-Tek O.C.T. | Sakura | Cat# 4583 |
| Triton X-100 | Sigma | Cat# X100 |
| Hoechst 33342 | ThermoFisher | Cat# 62249 |
| Prolong Gold anti-fade reagent | ThermoFisher | Cat# P36934 |
| Power SYBR green PCR Mastermix | Applied Biosystems | Cat# 4367660 |
| **Critical Commercial Assays** | | |
| SMARTer PCR cDNA synthesis kit | Clontech | Cat# 634926 |
| High-Capacity cDNA Reverse Transcription Kit | Applied Biosystems | Cat# 4374966 |
| PureLink RNA Mini kit | Invitrogen-ThermoFisher | Cat# 12183018A |
| RNEasy Micro kit | QIAGEN | Cat# 74004 |
| **Deposited Data** | | |
| scRNA seq | GEO | GEO: GSE162651 |
| Bulk RNA seq | GEO | GEO: GSE163003 |
| **Experimental Models: Organisms/Strains** | | |
| Mouse C57BL/6j | Jackson Laboratory | Cat# 000664 |
| Mouse *Flt3*-Cre;R26tdTomato | Dr. Kory Lavine (Lavine et.al., 2014) | N/A |
| Mouse *Ccr2*-GFP | Dr. Kory Lavine, Washington University School of Medicine | N/A |
| Mouse *Ccr2*-RFP | Dr. Kory Lavine, Washington University School of Medicine | N/A |
| Mouse *Cx3cr1*-GFP | Dr. Gwendolyn Randolph, Washington University School of Medicine | N/A |
| Mouse *CD115*-CreER;R26tdTomato | Dr. Gwendolyn Randolph, Washington University School of Medicine | N/A |
| Mouse *Clec4f*-Cre | Dr. Martin Guilliams (Bonnardel et al., 2019) | N/A |

(*Continued on next page*)

*Continued*

| REAGENT or RESOURCE | SOURCE | IDENTIFIER |
|---|---|---|
| **Oligonucleotides** | | |
| *36B4* For ATC CCT GAC GCA CCG CCG TGA | IDT | N/A |
| *36B4* Rev TGC ATC TGC TTG GAG CCC ACG TT | IDT | N/A |
| *Adgre1* For CTT TGG CTA TGG GCT TCC AGT | IDT | N/A |
| *Adgre1* Rev GCA AGG AGG ACA GAG TTT ATC GTG | IDT | N/A |
| *Timd4* For CCG GTG ACT TTG CCT TGT CAT | IDT | N/A |
| *Timd4* Rev CTC TGC ATT GCA CTT GGA ATT G | IDT | N/A |
| *CCL2* For *GGC TCA GCC AGA TGC AGTT AA* | IDT | N/A |
| *CCL2* Rev *CCT ACT CAT TGG GAT CAT CTT GCT* | IDT | N/A |
| *Cidec* For ATG GAC TAC GCC ATG AAG TCT | IDT | N/A |
| *Cidec* Rev CGG TGC TAA CAC GAC AGG G | IDT | N/A |
| *Colla1* For GCT CCT CTT AGG GGC CAC T | IDT | N/A |
| *Colla1* Rev CCA CGT CTC ACC ATT GGG G | IDT | N/A |
| *Trem2* For CTG GAA CCG TCA CCA TCA CTC | IDT | N/A |
| *Trem2* Rev CGA AAC TCG ATG ACT CCT CGG | IDT | N/A |
| *Gpnmb* For GCT GGT CTT CGG ATG AAA ATG A | IDT | N/A |
| *Gpnmb* Rev CCA CAA AGG TGA TAT TGG AAC CC | IDT | N/A |
| *CD63* For AGA GAC CAG GTG AAG TCA GAG | IDT | N/A |
| *CD63* Rev AGT CTG TGT AGT TAG AAG CTC CA | IDT | N/A |
| **Software and Algorithms** | | |
| FlowJo v10.7.1 | FlowJo | https://www.flowjo.com/ |
| GraphPad Prism 8 | GraphPad | https://www.graphpad.com/ |
| ImageJ | ImageJ | https://imagej.nih.gov/ij/ |
| Phantasus | Artyomov Lab, Washington University in St. Louis | https://artyomovlab.wustl.edu/phantasus/ |
| Single cell explorer | Artyomov Lab, Washington University in St. Louis | https://artyomovlab.wustl.edu/shiny//single_cell_explorer/ |
| R-package DESeq2 | RDocumentation | https://bioconductor.org/packages/release/bioc/html/DESeq2.html |
| R-package Seurat | RDocumentation | https://cran.r-project.org/web/packages/Seurat/index.html |
| **Other** | | |
| High fat, high sucrose diet | Research Diets | Cat# D12492 |
| FPC diet | Envigo | Cat# TD.190142 |

## RESOURCE AVAILABILITY

### Lead Contact

Further information and requests for resources and reagents should be directed to and will be fulfilled by the Lead Contact, Joel D. Schilling (schillij@wustl.edu).

### Materials Availability

This study did not generate new unique reagents.

### Data and Code Availability

Single cell RNA seq GEO: GSE162651, Bulk RNA seq GEO: GSE163003

## EXPERIMENTAL MODEL AND SUBJECT DETAILS

### *In vivo* animal studies

Wild-Type C57BL/6 male mice for the kinetic study were obtained from Jackson Laboratory. *Flt3*-Cre; R26tdTomato (Lavine et al., 2014), *Ccr2*-GFP and RFP mice (C57BL6/J background) were obtained from Dr. Kory Lavine. *Cx3cr1*-GFP, *CD115*-CreER; R26tdTomato (C57BL6/J background) were obtained from Dr. Gwendolyn Randolph. *Clec4f*-Cre mice were obtained from Martin Guilliams (Bonnardel et al., 2019). Mice were bred in house and littermates were used in the *Ccr2* WT versus KO studies. Mice of different genotypes were mixed in cages to reduce confounding by microbiota differences. All mice were maintained under pathogen free conditions. The high fat, high sucrose diet (HFD) containing 60% fat and 10% sucrose and was purchased from Research Diets (cat# D12492). The fructose, palmitate, cholesterol (FPC) diet containing 1.25% cholesterol was purchased from Envigo (cat# TD.190142). All animal protocols were approved by the Institutional Animal Care and Use Committee at Washington University School of Medicine, St. Louis. Male mice aged 8-12 weeks for used for all studies as female mice are protected from many of the high fat diet induced phenotypes.

### Human samples

Liver tissue was obtained from patients at the time of bariatric surgery who are currently a part of an ongoing investigation of liver metabolism with obesity (NCT003701828). All subjects provided written informed consent prior to sample collection. The study protocol was approved by the Human research Protection Office of Washington University School of Medicine, St. Louis, MO. We do not have information available about the gender of the subjects.

## METHOD DETAILS

### GTT and ITT

For the ITT mice were fasted for 6h after which they were given 0.75U/kg of insulin (Humulin) via IP injection. Blood glucose levels were obtained from tail vein blood at 30 min, 60 min, and 120 min using a glucometer. For GTT assessment, mice were fasted 16h and then given 2 g/kg body weight of 20% D-glucose (Sigma) via IP injection. Blood glucose levels were determined at baseline, 30 min, 60 min, and 120 min after injection using a glucometer.

### Single cell preparation of adipose and liver tissue for flow cytometry

After mice were euthanized the abdomen was exposed and the portal vein was cannulated via using a Terumo Sur-vet Surflo IV catheter (24G x $^{3}/_{4}$ "). Blood was subsequently drawn from the IVC for a plasma sample. The liver was then perfused with PBS via the portal vein for 3 min at a flow rate of 5 ml/min. After perfusion the liver was removed and 1 g was used for preparation of single cell suspension. The liver was minced and transferred to a tube continuing 15 mL of DMEM without serum, Collagenase D (1.6 mg/ml; Sigma) and DNase (50 μg/ml; Sigma) and then incubated with gentle rocking for 30 min at 37°C. The liver extract was mashed through a 70-micron filter and then the cell mixture was centrifuged at 50 rpm for 3 min to pellet the hepatocytes. The supernatant was then transferred to a new tube and centrifuged for 7 min at 900 rpm and this pellet was resuspended in 5 mL of 35% Percoll (Sigma) and then carefully added to 70% Percoll and centrifuged at 2200 rpm for 20 min with the brake turned off. The cells from the Percoll interface were removed and mixed with 10 mL of DMEM+10% serum and then the cells were pelleted. For liver analysis with FPC diet, a Percoll gradient was not employed. Adipose tissue macrophages were isolated from perigonadal fat pads that were minced and digested as above and then pelleted in the FACS buffer (2% BSA, EDTA in PBS). The cell pellets were then stained with Zombie Aqua (BioLegend) per manufacturer's instructions to discriminate live/dead cells. To prevent non-specific Fc binding, the cells were incubated with Fc Block (BD biosciences) for 10 min followed by the indicated antibody cocktail for 60 min in the dark on ice (CD45, CD11b, F4/80, TIM4, Ly6C, MHCII, CD11c). The samples were analyzed on a BD X20 flow cytometer and analyzed using FlowJo software (Version 10.3; Tree Star Inc). See Figure S1 for the gating strategy.

### Total RNA and qRT-PCR

A 50 mg piece of frozen liver was homogenized in Trizol and total RNA was isolated using a Purelink RNA mini kit (Invitrogen-Thermofisher). RNA was subjected to RT using a high capacity cDNA reverse transcription kit (Applied Biosystems). Real-time qRT-PCR was

performed using SYBR green reagent (Applied Biosystems) on an ABI 7500 fast thermocycler. Relative gene expression was determined using the delta-delta CT method normalized to 36B4 expression.

### Histology and Immunofluorescence

After perfusion, pieces of liver were placed in 10% neutral buffered formalin for 24h at 4°C followed by 70% ethanol and paraffin embedding. The paraffin embedded blocks were stained with H&E and picrosirius red at the Digestive Disease Research Core Center morphology core. Picrosirius red images were obtained at 4x with a Zeiss Akioskop brightfield microscope (average 10.8 ± 2.4 field of view/mouse) and picrosirius red area was quantified blinded with ImageJ using manual thresholding.

For IF, liver was fixed in 10% neutral buffered formalin for 24h, followed by 24h incubation in 30% sucrose and embedded in Tissue-Tek O.C.T. compound (Sakura). Eight μm thick cryosections were cut and mounted on glass slides. Sections were post-fixed in acetone/methanol (1:1) for 20 min at −20°C. Subsequently, sections were rehydrated for 5 min in water and washed 3 times with PBS. After blocking and permeabilization with blocking buffer (1% bovine serum albumin (BSA), 0.3% Triton X-100 in PBS) for 45 min, sections were incubated overnight with primary antibodies diluted in blocking buffer. Following the incubation, liver sections were washed 3 times with PBS and incubated with the appropriate secondary antibodies diluted in blocking buffer. Finally, sections were incubated with Hoechst 33342 (ThermoFisher Scientific), mounted with ProLong Gold anti-fade reagent (Invitrogen-ThermoFisher), and covered with #1.5 coverslips. Human liver sections were processed as described above. Lipid droplets were stained by monodansylpentane (MDH, Abcepta) using a similar staining protocol but without acetone/methanol fixation.

Images were obtained on a Zeiss LSM 700 laser scanning confocal microscope with 10x 0.3 N.A., 20x 0.8 N.A. objective or 63x oil immersion 1.4 NA objective. Analysis of macrophage aggregates or hCLS was done by manual counting of the number of aggregates/hCLS, aggregate/hCLS size (total number of cells/aggregate) and presence of C-LAMs (*Ccr2*-GFP-positive cells) per field of view acquired at 10x (average 11.1 ± 3.0 fields of view/mouse). A macrophage aggregate was defined by a minimum of three macrophages (identified by F4/80 and/or *Ccr2*-GFP positive staining) of which cell-to-cell contact was visible. Mature hCLSs were identified by a full ring structure formed by F4/80-positive and/or *Ccr2*-GFP positive macrophages.

### Transmission electron microscopy (TEM)

FACS sorted liver macrophage populations were fixed in 2% paraformaldehyde/2.5% glutaraldehyde (Polysciences Inc., Warrington, PA) in 100 mM sodium cacodylate buffer, pH 7.2 for 1h at room temperature. Samples were washed in sodium cacodylate buffer at room temperature and postfixed in 1% osmium tetroxide (Polysciences Inc.) for 1h. Samples were then rinsed extensively in $dH_20$ prior to en bloc staining with 1% aqueous uranyl acetate (Ted Pella Inc., Redding, CA) for 1h. Following several rinses in $dH_20$, samples were dehydrated in a graded series of ethanol and embedded in Eponate 12 resin (Ted Pella Inc.). Sections of 95 nm were cut with a Leica Ultracut UCT ultramicrotome (Leica Microsystems Inc., Bannockburn, IL), stained with uranyl acetate and lead citrate, and viewed on a JEOL 1200 EX transmission electron microscope (JEOL USA Inc., Peabody, MA) equipped with an AMT 8 megapixel digital camera and AMT Image Capture Engine V602 software (Advanced Microscopy Techniques, Woburn, MA).

### RNA sequencing

For single cell RNA sequencing (scRNA-seq) analysis of liver $CD45^{pos}$ cells from 3 mice fed a HFD for 20 wks were pooled and digested and isolated as described above. $CD45^{pos}$, $DAPI^{neg}$ were sorted using a FACSAriaIII (BD Biosciences). The cells were prepared and resuspended at a final concentration of $10^3$ cells/μl in PBS contain 0.04% BSA to minimize cell loss and aggregation. Approximately 20,000 cells were portioned into nanoliter-scale Gel bead-In-Emulsion (GEMs) to achieve single cell resolution for a maximum recovery of 10,000 individual cells. Utilizing the v2 Chromium Single Cell 3'' Library Kit and Chromium instrument (10X Genomics) poly-adenylated mRNA from an individual cell was tagged with a unique 16-bp 10X barcode and a 10-bp Unique Molecular Identifier (UMI). Full-length cDNA was then amplified to generate sufficient mass for library construction. Enzymatic fragmentation and size selection were used to optimize cDNA amplicon size (~400bp) for library construction. The final library is sequence ready and contains four unique sample indices. The concentration of the 10X single-cell library was accurate determine through qPCR to produce cluster counts appropriate for the HiSeq4000 platform (Illumina). Read lengths (26 × 98 nt) were generated targeting 50,000 reads per cell.

For bulk RNA-seq, single cell suspensions were prepared from the liver as described above from *Cx3cr1*$^{gfp/wt}$ mice feed a standard diet or HFD for 20 wks. Flow sorting was performed on an AriaIII cytometer and $CD45^{pos}$, $DAPI^{neg}$, $F4/80^{hi}$ cells that were either $TIM4^{pos}$ (KCs) or $TIM4^{neg}$; *Cx3cr1*$^{pos}$ (C-LAMs) were flow sorted into lysis buffer. RNA was isolated using microRNA isolation kit (QIAGEN) according to manufacturer's instructions. RNA quality and concentration were assessed using a bioanalyzer. The library preparation and sequencing were performed at the Genome Technology Access Center (GTAC) at Washington University School of Medicine. Briefly, the total cellular RNA was also prepared for RNA sequencing with the Clonetech SMARTer kit according to manufacturer's protocols, ligated with adapters and unique molecular indexes for each sample for every read, and then sequenced on one single-end 50bp lane on an Illumina HiSeq 3000. RNA-seq reads demultiplexed with Illumina's bcl2fastq2 and were then aligned to the *Mus musculus* Ensembl release 76 top-level assembly with STAR version 2.0.4b (Dobin et al., 2013). Gene counts were derived from the number of uniquely aligned unambiguous reads by Subread:featureCount version 1.4.5 (Liao et al., 2014). Sequencing performance was assessed for total number of aligned reads, total number of uniquely aligned reads, genes detected and ribosomal fraction, known junction saturation, and read distribution over known gene models with RSeQC version 2.3 (Wang et al., 2012).

All gene counts were then imported into the R/Bioconductor package EdgeR and TMM normalization size factors were calculated to adjust for differences in library size across all samples (McCarthy et al., 2012; Robinson et al., 2010). Ribosomal features as well as any feature not expressed in at least two samples above one count-per-million were excluded from further analysis and TMM size factors were recalculated to create effective TMM size factors. The effective TMM size factors and the matrix of counts were then imported into the R/Bioconductor package Limma and weighted likelihoods based on the observed mean-variance relationship of every gene and sample were then calculated for all samples with the voomWithQualityWeights function (Liu et al., 2015; Ritchie et al., 2015). Performance of the samples was assessed with a Pearson correlation matrix and multi-dimensional scaling plots. Generalized linear models were then created to test for differentially expressed genes. The results were then filtered for FDR adjusted p values less than or equal to 0.05. The results were then filtered for FDR adjusted p values less than or equal to 0.05. Gene set enrichment method was used to enhance the biological interpretation of differentially expressed genes by the help of R/Bioconductor package Fgsea (https://bioconductor.org/packages/release/bioc/html/fgsea.html). Principal component analysis was performed on top 12,000 most expressed genes as a technique to visualize the variation present in the dataset.

## QUANTIFICATION AND STATISTICAL ANALYSIS

Statistical analysis was performed using GraphPad Prism software. All results are expressed as means ± SE. For the comparison of two groups with normal distribution a Student's t test was employed. For analysis of genotype versus diet comparisons a 2-way ANOVA was employed to assess for interaction. Group sizes and number of independent experiments can be found in the figure legends. A value of $p \leq 0.05$ was considered significant.